

LOAN DOCUMENT

PHOTOGRAPH THIS SHEET

AD-A233 482

DTIC ACCESSION NUMBER

LEVEL

PHOTOGRAPH THIS SHEET

INVENTORY

WL-TR-91-3033 Vol II
DOCUMENT IDENTIFICATION
APR 1991

DISTRIBUTION STATEMENT A
Approved for public release;
Distribution Unlimited

DISTRIBUTION STATEMENT

H
A
N
D
L
E
W
I
T
H
C
A
R
E

ACCESSION FOR	
NTIS	GRA&I
DTIC	TRAC
UNANNOUNCED	
JUSTIFICATION	
BY	
DISTRIBUTION/	
AVAILABILITY CODES	
DISTRIBUTION	AVAILABILITY AND/OR SPECIAL
A-1	

DISTRIBUTION STAMP

DTIC
ELECTED
APR 11 1991
E D

DATE ACCESSIONED

DATE RETURNED

DATE RETURNED

91 4 10 147

DATE RECEIVED IN DTIC

REGISTERED OR CERTIFIED NUMBER

REGISTERED OR CERTIFIED NUMBER

PHOTOGRAPH THIS SHEET AND RETURN TO DTIC-FDAC

WL-TR-91-3033
Volume I

AD-A233 482



CALCULATION OF HIGH ANGLE OF ATTACK AERODYNAMICS
OF FIGHTER CONFIGURATIONS; VOLUME I-STEADY

C. Edward Lan, H. Emdad, Swei Chin
P. Sundaram, S. C. Mehrotra, and
R. K. Tripathi

Vigyan Research Associates, Inc.
30 Research Dr
Hampton VA 23666-1325

April 1991

Final Report for Period Aug 87 - Jan 90

Approved for public release; distribution is unlimited.

FLIGHT DYNAMICS DIRECTORATE
WRIGHT LABORATORY
AIR FORCE SYSTEMS COMMAND
WRIGHT-PATTERSON AIR FORCE BASE, OHIO 45433-6553

NOTICE

When Government drawings, specifications, or other data are used for any purpose other than in connection with a definitely Government-related procurement, the United States Government incurs no responsibility or any obligation whatsoever. The fact that the government may have formulated or in any way supplied the said drawings, specifications, or other data, is not to be regarded by implication, or otherwise in any manner construed, as licensing the holder, or any other person or corporation; or as conveying any rights or permission to manufacture, use, or sell any patented invention that may in any way be related thereto.

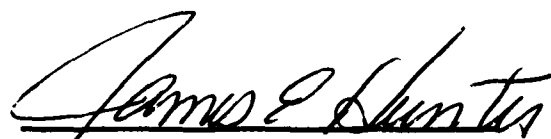
This report is releasable to the National Technical Information Service (NTIS). At NTIS, it will be available to the general public, including foreign nations.

This technical report has been reviewed and is approved for publication.



CHARLES B. HEATH
DesignPredictions Group

FOR THE COMMANDER



JAMES E. HUNTER
Flight Control Division

If your address has changed, if you wish to be removed from our mailing list, or if the addressee is no longer employed by your organization please notify WL/FIGC, WPAFB, OH 45433-6553 to help us maintain a current mailing list.

Copies of this report should not be returned unless return is required by security considerations, contractual obligations, or notice on a specific document.

8c. ADDRESS (City, State, and ZIP Code)			10. SOURCE OF FUNDING NUMBERS			
			PROGRAM ELEMENT NO.	PROJECT NO.	TASK NO.	WORK UNIT ACCESSION NO.
			65502F	3005	40	09
11. TITLE (Include Security Classification) Calculation of High Angle of Attack Aerodynamics of Fighter Configurations; Volume I-Steady						
12. PERSONAL AUTHOR(S) C. E. Lan, H. Emdad, S. Chin, P. Sundaram, S. C. Mehrotra, and R. K. Tripathy						
13a. TYPE OF REPORT		13b. TIME COVERED		14. DATE OF REPORT (Year, Month, Day)		15. PAGE COUNT
Final		FROM <u>Aug 87</u> TO <u>Jan 90</u>		April 1991		82
16. SUPPLEMENTARY NOTATION This is a Small Business Innovative Research Program, Phase II report.						
17. COSATI CODES			18. SUBJECT TERMS (Continue on reverse if necessary and identify by block number)			
FIELD	GROUP	SUB-GROUP	Stability and Control			
			High Angle of Attack Aerodynamics			
19. ABSTRACT (Continue on reverse if necessary and identify by block number) A computational method for lateral-directional aerodynamics of fighter configurations is developed. The leading-edge vortices are represented by free vortex filaments which are adjusted iteratively to satisfy the force-free condition. The forebody vortex separation, both symmetrical and asymmetrical, is calculated using slender body theory. Effect of boundary layer separation on lifting surfaces is accounted for using the effective sectional angles of attack. The latter are obtained iteratively by matching the nonlinear sectional lift with the computed resulted based on lifting-surface theory. Results for several fighter configurations are employed for comparison with available data. It is shown that the present method produces reasonable results in predicting sideslip derivatives, while roll- and yaw-rate derivatives do not compare very well with forced oscillation test data at high angles of attack. Industrial usage of this has produced mixed results. At this time, the use of these methods in a production manner is not recommended.						
20. DISTRIBUTION / AVAILABILITY OF ABSTRACT <input checked="" type="checkbox"/> UNCLASSIFIED/UNLIMITED <input type="checkbox"/> SAME AS RPT. <input type="checkbox"/> DTIC USERS				21. ABSTRACT SECURITY CLASSIFICATION Unclassified		
22a. NAME OF RESPONSIBLE INDIVIDUAL CHARLES B. HEATH				22b. TELEPHONE (Include Area Code) (513) 255-8489		22c. OFFICE SYMBOL WL/FIGC

ABSTRACT

A computational method for lateral-directional aerodynamics of fighter configurations is developed. The leading-edge vortices are presented by free vortex filaments which are adjusted iteratively to satisfy the force-free condition. The forebody vortex separation, both symmetrical and asymmetrical, is calculated with a slender body theory. Effect of boundary layer separation on lifting surfaces is accounted for by using the effective sectional angles of attack. The latter are obtained iteratively by matching the nonlinear sectional lift with the computed results based on a lifting-surface theory. Results for several fighter configurations are employed for comparison with available data. It is shown that the present method produces reasonable results in predicting sideslip derivatives, while roll- and yaw-rate derivatives do not compare very well with forced-oscillation test data at high angles of attack.

LIST OF SYMBOLS

b	span
c	local chord
\bar{c}	mean aerodynamic chord
C, C'	sectional leading-edge singularity parameter
c_A	sectional axial force coefficient
c_d	sectional drag coefficient
C_D	drag coefficient
C_{D_i}	induced drag coefficient
c_l	sectional lift coefficient
C_L	total lift coefficient
C_{ℓ}	rolling moment coefficient
C_{ℓ_β}	$\partial C_\ell / \partial \beta$
C_{ℓ_p}	$\partial C_\ell / \partial \bar{p}$
C_{ℓ_r}	$\partial C_\ell / \partial \bar{r}$
c_m	sectional pitching moment coefficient
C_m	total pitching moment coefficient
c_n	sectional normal force coefficient
C_n	yawing moment coefficient
C_{n_β}	$\partial C_n / \partial \beta$
C_N	body normal force coefficient based on maximum cross-sectional area
C_p	pressure coefficient
ΔC_p	lifting pressure coefficient
c_s	sectional leading-edge suction coefficient
\bar{c}_s	$c c_s / \bar{c} \sin^2 \alpha$
c_t	sectional leading-edge thrust coefficient

$\vec{e}_r, \vec{e}_\theta$	unit vectors in cylindrical coordinate system (see fig. 4)
f	ratio of sectional lift coefficients from 2-D to 3-D calculations
$\vec{i}, \vec{j}, \vec{k}$	unit vectors in the x,y,z directions, respectively
l	leading-edge length
k	residual vortex lift factor
M	mach number
\vec{n}	unit normal vector
N	number of chordwise vortex elements in a strip
p	roll rate
\bar{p}	$pb/2V_\infty$
q	pitch rate
r	radial coordinate or yaw rate
\bar{r}	$rb/2V_\infty$
r_0	leading-edge radius
R	body radius
S	reference area
u,v,w	induced velocity components along x,y,z coordinates, respectively
\vec{V}	total velocity vector
V_n	induced normal velocity
V_∞	freestream velocity
x,y,z	cartesian coordinates with x being positive pointing downstream, a positive y pointing to the right, and a positive z pointing upwards
$\Delta \bar{x}$	nondimensional x-distance from the trailing edge to the vortex breakdown point
\bar{y}_{BD}	spanwise location of vortex breakdown point nondimensionalized with respect to half span
\bar{y}_c	nondimensional centroid location of the \bar{c}_s -distribution from inboard to η of $\bar{c}_{s(max)}$

\bar{y}_l distance from apex to centroid of \bar{c}_s -distribution from inboard to η of $\bar{c}_{s(\max)}$, measured along the leading edge and referred to half span
 z complex variable
 z_c camber surface ordinate
 z_t thickness ordinate

Greek

α angle of attack
 α_o sectional angle of attack
 α_{BD} α for vortex breakdown at the trailing edge in symmetrical loading
 α_e effective angle of attack
 α_s angle of attack of initial vortex separation
 α_{tw} difference in angles of attack at tip and root sections, negative for washout
 β sideslip angle, or $\sqrt{1 - M^2}$
 δ_N nose angle of a wedge section
 η $y/b/2$
 Γ sectional circulation or vortex strength
 γ_x nondimensional streamwise vortex density
 γ_y or γ nondimensional spanwise vortex density
 Λ sweep angle
 ϕ geometric dihedral
 ϕ velocity potential
 ρ density
 σ source strength
 ψ sweep angle of a vortex element
 θ angular coordinate of a body cross section
 ζ complex variable

Subscript

α	due to α in symmetrical loading
β	sideslip
BR	vortex breakdown on the right wing
BL	vortex breakdown on the left wing
f	fuselage
l	leading edge
max	maximum
n	normal direction
p	roll rate
r	yaw rate
t	tip or trailing edge
tw	twist
w	wing
z	normal to a planform
∞	freestream

1. INTRODUCTION

Maneuvering flight at high angles of attack may induce boundary-layer separation and vortex-separated flow over aerodynamic surfaces. In addition, the usually well-organized vortex flow may also break down at a high enough angle of attack. These flow phenomena affect not only the individual aerodynamic surfaces on which these phenomena occur but also those in their close proximity. These flow patterns are now well known qualitatively for fighter configurations from extensive wind and water tunnel tests. However, development of quantitative prediction methods has not kept pace with tunnel testing.

Ultimately, a theoretical method for predicting aerodynamics at high angles of attack would be ideally based on Navier-Stokes solutions with appropriate turbulence modeling. However, for applications to preliminary design, this is not feasible at the present time due to inadequate computer resources. Therefore, a practical approach would be one involving panel or panel-like methods with corrections for high angle-of-attack flow features. For example, one currently available computer code for complete aircraft configurations is the PAN AIR (refs. 1 and 2). This code is based on the solution of the Prandtl-Glauert equation and may include boundary-layer corrections. However, its applications to configurations with extensive boundary-layer separation or vortex flow have not been demonstrated. It should be noted that symmetrical vortex flow without breakdown on simple configurations has been dealt with successfully in reference 3 based on a panel method. Similarly, the VSAERO code (refs. 4 and 5) was developed mainly for symmetrical flight conditions with vortex flow and boundary-layer correction at moderate angles of attack. A comprehensive method for lateral-

directional aerodynamics with aeroelastic effect is that of the FLEXSTAB (ref. 6). However, it was valid only in the region of linear aerodynamics, and hence at low angles of attack. Recently, the VSAERO code has been extended to enable calculation of stability and control characteristics of airplanes (ref. 7). Again, applications to high angle-of-attack aerodynamics have not been reported.

To remedy the inadequacy of existing methods, particularly in the area of nonlinear lateral-directional aerodynamics, the VORSTAB code was developed for vortex-dominated configurations (refs. 8 and 9). In this code, the effect of vortex lift is included through the method of suction analogy while the effect of vortex breakdown has been accounted for using a theoretical correlation parameter obtained from experimental data. The code can treat conventional fighter configurations by using nonlinear section data for the effect of boundary-layer separation (ref. 10). Either could be used in the code experimental or theoretical nonlinear section data in order to avoid extreme difficulty in the theoretical prediction of three-dimensional viscous separated flows.

In the present investigation, the method of suction analogy used in reference 8 is replaced with the method of free vortex filaments (ref. 11) to allow a more accurate calculation of interference effects among different lifting surfaces. In addition, forebody vortex separation on noncircular cross sections is also modeled. The results obtained demonstrate the promise of the present code on a design tool.

In this report both the theoretical and empirical methods used in the code will be described. Numerical results to demonstrate the applicability of the present code to modern fighter aircraft geometries will be presented.

2. THEORETICAL APPROACHES

2.1. General Concept

The main flow features accounted for in the present method are illustrated in Figure 1. The basic flow considered in the code is the subsonic potential flow, with corrections for boundary-layer separation and imbedded free vortex filaments for vortex flow effect. The potential flow calculation is based on the small disturbance approximation of the gas dynamic equations which result in the Prandtl-Glauert equation. There are two kinds of flow singularities used in the program: horseshoe vortices for lifting surfaces and vortex multiplets for the fuselage. The strength of the singularities can be obtained by satisfying the boundary conditions on the fuselage and lifting surfaces. To properly account for the leading-edge singularity of pressure loading in the linear theory, and hence the leading-edge thrust, the Quasi-Vortex-Lattice Method (QVLM) is used (ref. 12).

In addition, the vortex flow arising from separation along the leading and side edges of a low aspect ratio wing which significantly affects the high angle-of-attack aerodynamics is simulated by using discrete free vortex filaments emanating from the edges. At a high enough angle of attack, the vortex flow will breakdown and decrease the vortex lift effect. The latter is calculated in the present method by using empirical formulas derived from the analysis of experimental data.

Another phenomenon limiting the high angle-of-attack flight envelopes for high performance aircraft is the boundary-layer separation. To account for this viscous effect on the lifting surfaces, sectional nonlinear data are used iteratively. In the following, the various methodologies used in the code will be summarized.

2.2. Potential Flow Theory

As indicated earlier, the present potential flow method is based on the solution of the Prandtl-Glauert equation:

$$(1 - M_{\infty}^2) \frac{\partial^2 \Phi}{\partial x^2} + \frac{\partial^2 \Phi}{\partial y^2} + \frac{\partial^2 \Phi}{\partial z^2} = 0 \quad (1)$$

where Φ is the perturbation velocity potential. The solution is represented by vortex distributions. The thin wing approximation is used throughout.

2.2.1. Boundary Conditions

Lifting Surfaces. The boundary condition for the Prandtl-Glauert equation on the wing is that the velocity component normal to the wing surface should be zero. Assuming that the wing surface can be described as

$$z = z_c(x, y) \quad (2)$$

The unit normal vector on the wing surface can be written as

$$\vec{n} = \frac{-\frac{\partial z_c}{\partial x} \vec{i} - \frac{\partial z_c}{\partial y} \vec{j} + \vec{k}}{\sqrt{1 + \left(\frac{\partial z_c}{\partial x}\right)^2 + \left(\frac{\partial z_c}{\partial y}\right)^2}} \quad (3)$$

For an airplane having angular motions with rates p , q , and r being positive along the positive x' , y' and z' -direction, respectively (see fig. 2 for coordinate systems), the onset velocity at (x', y', z') relative to the airplane due to these angular rates is

$$-(\vec{i}p + \vec{j}q + \vec{k}r) \times (\vec{i}x' + \vec{j}y' + \vec{k}z') = -\vec{i}(qz' - ry') + \vec{j}(pz' - rx') - \vec{k}(py' - qx')$$

To express this velocity vector in the aerodynamic coordinate system (x, y, z) , the sign of \vec{i} and \vec{k} components must be reversed and x' , y' and z' are to be replaced by $-x$, y , and $-z$, respectively. It follows that

$$\vec{v} = \vec{i}(-qz - ry) + \vec{j}(-pz + rx) + \vec{k}(py + qx)$$

This must be added to the induced velocity (u, v, w) due to a vortex distribution and the uniform freestream contribution due to angle of attack (α) and sideslip (β) to obtain the total velocity vector at (x, y, z) :

$$\begin{aligned} \vec{V} = & (V_{\infty} \cos \alpha - qz - ry + u)\vec{i} + (-V_{\infty} \sin \beta - pz + rx + v)\vec{j} \\ & + (V_{\infty} \sin \alpha + py + qx + w)\vec{k} \end{aligned} \quad (4)$$

Applying the tangency condition

$$\vec{V} \cdot \vec{n} = 0 \quad (5)$$

the boundary condition becomes

$$\begin{aligned} w - v \frac{\partial z_c}{\partial y} = & (V_{\infty} \cos \alpha - qz - ry) \frac{\partial z_c}{\partial x} \\ & + (-V_{\infty} \sin \beta - pz + rx) \frac{\partial z_c}{\partial y} - V_{\infty} \sin \alpha - py - qx \end{aligned} \quad (6)$$

where $u \partial z_c / \partial x$ has been ignored as a second-order term. For a wing with dihedral (ϕ) and twist (α_{tw}) , it can be shown that (ref. 13)

$$\frac{\partial z_c}{\partial x} = \frac{-\sin \alpha_{tw} + \frac{dz_c}{dx_2} \cos \alpha_{tw}}{\cos \phi \left(\cos \alpha_{tw} + \frac{dz_c}{dx_2} \sin \alpha_{tw} \right)} \quad (7a)$$

$$\frac{\partial z_c}{\partial y} = \frac{\sin \phi \cos \alpha_{tw} + \frac{dz_c}{dy_2} \cos \phi}{\cos \phi \left(\cos \alpha_{tw} - \frac{dz_c}{dy_2} \sin \phi \right)} \quad (7b)$$

where the (x_2, y_2) coordinate system is illustrated in Figure 3. Basically, it is a coordinate system based on the local wing chord plane in a nonplanar configuration. For a cambered wing with small spanwise slopes (dz_c/dy_2) , it can be shown from equation (7b) that

$$\frac{\partial z_c}{\partial y} \approx \tan \phi \quad (8)$$

Therefore, the wing boundary condition becomes

$$\begin{aligned} V_n &= \frac{w}{V_\infty} \cos \phi - \frac{v}{V_\infty} \sin \phi = V_{nw} + V_{nf} = \cos \phi \frac{\partial z_c}{\partial x} \cos \alpha - \sin \alpha \cos \phi \\ &\quad - \sin \beta \sin \phi - \left(\frac{pb}{2V_\infty} \right) \frac{2}{b} (z \sin \phi + y \cos \phi) \\ &\quad + \left(\frac{rb}{2V_\infty} \right) \frac{2}{b} \left(x \sin \phi - y \cos \phi \frac{\partial z_c}{\partial x} \right) \\ &\quad - \left(\frac{qc}{2V_\infty} \right) \frac{2}{c} \left(x + z \frac{\partial z_c}{\partial x} \right) \cos \phi \end{aligned} \quad (9)$$

where V_{nw} is the induced normal velocity due to the vortex distribution of lifting surfaces and V_{nf} is that due to the fuselage and \bar{c} in the mean aerodynamic chord.

Fuselage. The fuselage surface will be described with the following expression:

$$F(r, \theta, x) = r - R(\theta, x) \quad (10)$$

where the coordinate system is shown in Figure 4. It follows that the normal vector on the surface in cylindrical coordinate system with $\vec{e}_r, \vec{e}_\theta$ as basis vectors is given by

$$\vec{\nabla}F = \vec{e}_r - \vec{e}_\theta \frac{1}{R} \frac{\partial R}{\partial \theta} - \vec{i} \frac{\partial R}{\partial x} = \vec{e}_r + \vec{e}_\theta \frac{1}{R} \frac{\partial R}{\partial \theta} - \vec{i} \frac{\partial R}{\partial x} \quad (11)$$

The total velocity vector is still given by equation (4). As shown in Figure 3 the unit vectors, \vec{j} and \vec{k} , are related to the basis vectors, \vec{e}_r and \vec{e}_θ in the following way:

$$\begin{bmatrix} \vec{j} \\ \vec{k} \end{bmatrix} = \begin{bmatrix} \sin \theta & -\cos \theta \\ \cos \theta & \sin \theta \end{bmatrix} \begin{bmatrix} \vec{e}_r \\ \vec{e}_\theta \end{bmatrix} \quad (12)$$

Therefore, the total velocity vector can be rewritten as

$$\begin{aligned} \vec{V} = & (V_\infty \cos \alpha - qz - ry + u)\vec{i} + [v \sin \theta + w \cos \theta + rx \sin \theta + qx \cos \theta \\ & + p(y \cos \theta - z \sin \theta) - V_\infty \sin \beta \sin \theta + V_\infty \sin \alpha \cos \theta]\vec{e}_r \\ & + [v \cos \theta - w \sin \theta + rx \cos \theta + qx \sin \theta + p(y \sin \theta + z \cos \theta) \\ & + V_\infty \sin \beta \cos \theta + V_\infty \sin \alpha \sin \theta]\vec{e}_\theta \end{aligned} \quad (13)$$

Applying the boundary condition:

$$\vec{v} \cdot \vec{\nabla} \bar{F} = 0,$$

it is obtained that

$$\begin{aligned} \frac{v_r}{V_\infty} - \frac{v_\theta}{V_\infty} \frac{1}{R} \frac{\partial R}{\partial \theta} &= \cos \alpha \frac{\partial R}{\partial x} - \sin \alpha \cos \theta - \sin \alpha \sin \theta \frac{1}{R} \frac{\partial R}{\partial \theta} \\ &+ \sin \beta \sin \theta - \sin \beta \cos \theta \frac{1}{R} \frac{\partial R}{\partial \theta} \\ &- \left(\frac{pb}{2V_\infty} \right) \left[\frac{y \cos \theta - z \sin \theta}{b/2} + \frac{y \sin \theta + z \cos \theta}{b/2} \frac{1}{R} \frac{\partial R}{\partial \theta} \right] \\ &+ \left(\frac{rb}{2V_\infty} \right) \left[- \frac{x \sin \theta}{b/2} - \frac{x \cos \theta}{b/2} \frac{1}{R} \frac{\partial R}{\partial \theta} - \frac{y}{b/2} \frac{\partial R}{\partial x} \right] \\ &+ \left(\frac{qc}{2V_\infty} \right) \left[\frac{x \cos \theta}{c/2} + \frac{x \sin \theta}{c/2} \frac{1}{R} \frac{\partial R}{\partial \theta} - \frac{z}{c/2} \frac{\partial R}{\partial x} \right] \end{aligned} \quad (14)$$

where

$$v_r = v \sin \theta + w \cos \theta$$

$$v_\theta = v \cos \theta - w \sin \theta$$

It should be noted that the term associated with $(pb/2V_\infty)$ can be simplified because with $y = R \sin \theta$ and $z = R \cos \theta$,

$$y \cos \theta - z \sin \theta = 0 \quad (15a)$$

$$y \sin \theta + z \cos \theta = R \quad (15b)$$

2.2.2. Vortex Distributions on Lifting Surfaces

To satisfy the Prandtl-Glauert equation (1) and the boundary condition (eq. 9), surface vortex distributions on lifting surfaces and the wake are used to produce an induced velocity vector at any point (\vec{R}) in the field given by

$$\vec{v}(\vec{R}) = \frac{\beta^2}{4\pi} \int_S \frac{(\vec{R}_1 - \vec{R}) \times \vec{\omega}(\vec{R}_1)}{R_\beta^2} ds \quad (16)$$

where

$$\vec{R} = x\vec{i} + y\vec{j} + z\vec{k}$$

$$R_\beta^2 = (x-x_1)^2 + \beta^2(y-y_1)^2 + \beta^2(z-z_1)^2 \quad (17)$$

and $\vec{\omega}$ is the vorticity vector at $\vec{R}_1 = x_1\vec{i} + y_1\vec{j} + z_1\vec{k}$. Equation (16) is to be substituted into equation (9) to obtain an equation for the unknown $\vec{\omega}$. To simplify the arithmetic, a typical procedure is to reduce the integral in equation (16) to a finite sum through a panel method or a vortex-lattice method. In the present code, a method called the quasi-vortex-lattice method (QVLM) is used to sum the effect of horseshoe vortices (ref. 12). The QVLM methodology was developed to accurately account for mathematical singularities of the square-root type at the leading edges and the Cauchy type in the chord-wise integral. Accurate calculation of the leading-edge thrust is needed in calculating the vortex-flow effect (see section 2.3.1).

To illustrate the essential idea of the QVLM, consider a thin airfoil in a two-dimensional flow. The induced velocity at x on the chord line is

$$w(x,0) = -\frac{1}{2\pi} \int_0^1 \frac{\gamma(\xi)d\xi}{x-\xi} \quad (18)$$

The integrand in equation (18) possesses a Cauchy singularity at $\xi = x$. In addition, $\gamma(\xi)$ has a square-root singularity at $\xi = 0$. To eliminate the square-root singularity, the x -coordinate is transformed to a θ -coordinate through the following relation:

$$x = \frac{(1 - \cos \theta)}{2} \quad (19)$$

$$\xi = \frac{(1 - \cos \theta')}{2} \quad (20)$$

Therefore, equation (18) becomes

$$w(\theta) = \frac{1}{2\pi} \int_0^\pi \frac{\gamma(\theta') \sin \theta' d\theta'}{\cos \theta - \cos \theta'} \quad (21)$$

Let

$$g(\theta) = \gamma(\theta) \sin(\theta) \quad (22)$$

Since $\gamma(\theta)$ has a square-root singularity at $\theta = 0$ and $\sin \theta$ vanishes at $\theta = 0$ as \sqrt{x} , the square-root singularity of $\gamma(\theta)$ is eliminated by the factor $\sin \theta$. Equation (21) can be written as

$$w(\theta) = \frac{1}{2\pi} \int_0^\pi \frac{g(\theta') - g(\theta)d\theta}{\cos \theta - \cos \theta'} \quad (23)$$

Equation (23) can now be reduced to a finite sum through the midpoint trapezoidal rule as follows:

$$w(x_i) = \frac{-1}{2N} \sum_{k=1}^N \left(\frac{\gamma_k x_k (1 - x_k)^{1/2}}{x_i - x_k} \right) + \begin{cases} NC, & i = 0 \\ 0, & i \neq 0 \end{cases} \quad (24)$$

where

x_i is x at $\theta_i - i\pi/N$

x_k is at $\theta_k = (2k - 1)\pi/2N$

where C is related to the frequently-used leading-edge singularity parameter C'

$$C' = \lim_{x \rightarrow 0} u(x) \sqrt{x} = \lim_{x \rightarrow 0} \frac{1}{2} \gamma(x) \sqrt{x} = \frac{C}{2} \quad (25)$$

and can be computed once γ_k 's are obtained.

In a three-dimensional flow, the wing surface with a leading edge sweep Λ_λ is divided into vortex strips. Over each vortex strip, the vortex integral is reduced to a finite sum in exactly the same manner as in the thin airfoil case described above with the leading-edge singularity parameter C calculated from the following relation (ref. 12):

$$NC \sqrt{\tan^2 \Lambda_\lambda + \beta^2} = \int (\text{induced upwash at l.e.}) \\ - \left[\cos \phi \frac{\partial z}{\partial x} \cos \alpha - \cos \phi \sin \alpha \right] \quad (26)$$

The sectional leading-edge thrust coefficient (c_t) is then given by

$$c_t = \frac{\pi C^2 \sqrt{1 - M_\infty^2 \cos^2 \Lambda_\lambda}}{2 \cos \Lambda_\lambda} \quad (27)$$

Detailed expressions for the induced velocity vector to be used in the boundary conditions can be found in reference 12.

2.2.3. Distribution of Vortex Multiplets for the Fuselage Effect

For the fuselage effect, G. N. Ward's vortex multiplets are distributed along the fuselage axis (ref. 14). The velocity potential is given by

$$\frac{1}{V_\infty} \phi_f(x, \theta, r) = -\frac{1}{4\pi} \sum_n \left\{ \begin{array}{l} \cos n\theta \\ \sin n\theta \end{array} \right\} \int_{x_{f\ell}}^{x_{ft}} \frac{[x-\xi + \sqrt{(x-\xi)^2 + \beta^2 r^2}]^n}{r^n \sqrt{(x-\xi)^2 + \beta^2 r^2}} f_n(\xi) d\xi \quad (28)$$

where $\cos n\theta$ is for the symmetrical loading and $\sin n\theta$ for the antisymmetrical loading. In an asymmetrical flow, such as in a lateral or directional motion, both terms are needed. To use equation (28), the integral is first integrated by parts and the resulting expression for ϕ_f is then differentiated to obtain V_r and V_θ as follows:

$$\begin{aligned} \left(\frac{V_r}{V_\infty}\right)_f &= \frac{1}{V_\infty} \frac{\partial \phi_f}{\partial r} = -\frac{1}{4\pi} \sum_n \left\{ \begin{array}{l} \cos n\theta \\ \sin n\theta \end{array} \right\} \left\{ f_n(x_{ft}) \frac{\partial F_n}{\partial r}(x_{ft}) - f_n(x_{f\ell}) \frac{\partial F_n}{\partial r}(x_{f\ell}) \right. \\ &\quad \left. + \int_{x_{f\ell}}^{x_{ft}} \frac{\partial F_n}{\partial r}(\xi) f_n'(\xi) d\xi \right\} \end{aligned} \quad (29)$$

$$\begin{aligned} \left(\frac{V_\theta}{V_\infty}\right)_f &= \frac{1}{V_\infty} \frac{\partial \phi_f}{r \partial \theta} = -\frac{1}{4\pi} \frac{1}{r} \sum_n \left\{ \begin{array}{l} -n \sin n\theta \\ n \cos n\theta \end{array} \right\} \left\{ f_n(x_{ft}) F_n(x_{ft}) - f_n(x_{f\ell}) F_n(x_{f\ell}) \right. \\ &\quad \left. + \int_{x_{f\ell}}^{x_{ft}} F_n(\xi) f_n'(\xi) d\xi \right\} \end{aligned} \quad (30)$$

where

$$F_n(\xi) = -\frac{1}{n} \frac{[x - \xi + \sqrt{(x-\xi)^2 + \beta^2 r^2}]^n}{r^n}, \quad n \neq 0$$

$$= -\lambda_n \frac{x - \xi + \sqrt{(x-\xi)^2 + \beta^2 r^2}}{\beta r}, \quad n = 0 \quad (31)$$

$$\frac{\partial F_n}{\partial r} = \frac{x - \xi}{r} \frac{[(x-\xi) + \sqrt{(x-\xi)^2 + \beta^2 r^2}]^n}{r^n \sqrt{(x-\xi)^2 + \beta^2 r^2}}, \quad n \geq 0. \quad (32)$$

When equations (29) and (30) are substituted into the boundary condition (eq. (14)), the resulting equation becomes an integral equation for the unknown singularity strength $f_n^-(\xi)$. The integrals involving $f_n^-(\xi)$ are reduced to finite sums as follows:

$$\int_{x_{f\ell}}^{x_{ft}} \frac{\partial F_n}{\partial r} f_n^- d\xi \approx (x_{ft} - x_{f\ell}) \frac{\pi}{2N_F} \sum_k f_{nk}^- \sin \theta_k \frac{\partial F_{nk}}{\partial r} \quad (33)$$

$$\int_{x_{f\ell}}^{x_{ft}} F_n f_n^- d\xi \approx (x_{ft} - x_{f\ell}) \frac{\pi}{2N_F} \sum_k f_{nk}^- \sin \theta_k F_{nk} \quad (34)$$

$$\xi = x_{f\ell} + (x_{ft} - x_{f\ell})(1 - \cos \theta)$$

$$\theta_k = (2k - 1) \frac{\pi}{4N_F}$$

The transformation used between ξ and θ is to transform $\xi = (x_{f\ell}, x_{ft})$ into $\theta = (0, \pi/2)$.

The boundary condition (eq. 14) is to be satisfied on the surface. For this purpose, the method of weighted residuals will be used with $R_i^{m+1} \cos m\theta$ as the weighting function, where $R_i(x_i, \theta)$ is the radius function at a

control station x_i . Now equation (14) is multiplied by $R_i^{m+1} \cos m\theta$ and integrated from $-\pi$ to π , where $m=0,1,\dots$. For example, in a symmetrical case with $m=0$:

$$\begin{aligned} \frac{1}{2\pi} \int_{-\pi}^{\pi} \frac{v_r}{V_{\infty}} R_i d\theta - \frac{1}{2\pi} \int_{-\pi}^{\pi} \frac{v_{\theta}}{V_{\infty}} \frac{1}{R_i} \frac{\partial R_i}{\partial \theta} R_i d\theta &= \cos \alpha \frac{1}{2\pi} \int_{-\pi}^{\pi} R_i \frac{\partial R_i}{\partial x} d\theta \\ - \sin \alpha \frac{1}{2\pi} \int_{-\pi}^{\pi} \sin \theta \frac{1}{R_i} \frac{\partial R_i}{\partial \theta} R_i d\theta - \sin \alpha \frac{1}{2\pi} \int_{-\pi}^{\pi} \cos \theta R_i d\theta, \\ & i=1, \dots, N_F. \end{aligned} \quad (35)$$

Similarly, for $m=1$,

$$\begin{aligned} \frac{1}{2\pi} \int_{-\pi}^{\pi} \frac{v_r}{V_{\infty}} R_i^2 \cos \theta d\theta - \frac{1}{2\pi} \int_{-\pi}^{\pi} \frac{v_{\theta}}{V_{\infty}} \frac{1}{R_i} \frac{\partial R_i}{\partial \theta} R_i^2 \cos \theta d\theta &= \cos \alpha \frac{1}{2\pi} \int_{-\pi}^{\pi} R_i^2 \frac{\partial R_i}{\partial x} \\ \cdot \cos \theta d\theta - \frac{\sin \alpha}{2\pi} \int_{-\pi}^{\pi} \cos \theta R_i^2 \cos \theta d\theta \\ - \frac{\sin \alpha}{2\pi} \int_{-\pi}^{\pi} \sin \theta \frac{1}{R_i} \frac{\partial R_i}{\partial \theta} R_i^2 \cos \theta d\theta, & i=1, \dots, N_F. \end{aligned} \quad (36)$$

Note that v_r and v_{θ} include both fuselage and wing effects. Equations (35), (36), etc. are used to solve for the unknowns f_n' . For a fuselage with finite slope at the nose, $f_n(x_{fl}) = 0$.

It should be noted that when a combination of surface and axial vortex distributions is used, the wing loading may become too low at the wing-fuselage juncture due to the horseshoe-vortex discretization of wing vortex distributions. This problem is solved in the present code, under the symmetrical loading condition, by eliminating the inboard trailing vortices

associated with the root vortex strip. If this is not done, the root vortex strip will exhibit a loading similar to that near the wing tip.

A more detailed derivation of equations for a body of revolution can be found in reference 15.

2.3. Vortex Flow Theory

When a lifting surface is assumed to exhibit edge-separated vortex flow, free vortex filaments emanating from these edges are employed to simulate the induced aerodynamic effect (ref. 11). The strength of these free vortex filaments is affected by the leading-edge radius, wing thickness, boundary layer separation, and vortex breakdown. In addition, forebody vortices may produce significant effect on overall aerodynamic characteristics of a configuration. Theoretical methods to calculate these effects are discussed in the following.

2.3.1. Free Vortex Filaments (Reference 11)

The idea of using free vortex filaments for leading edge separated flow was described in reference 11. A typical vortex filament is shown in Figure 5. A filament consists of a series of short straight segments. The initial location of these segments is shown in dashed lines and the final location in solid lines. Points A through E lie along a wing trailing vortex element. BC is allowed to move only in the free stream direction, whereas CD is fixed in the wing plane because the flow is tangential to the trailing edge. DE is also fixed in the wing plane. Both segments AB and IJ are allowed to move to align with the local velocity vector.

In addition to the force-free condition on all free vortex elements, boundary conditions are also satisfied along the leading edges. These conditions are related to the degree of vortex separation. Note that the amount of residual leading-edge thrust can be used as a measure of the degree of vortex separation. In other words, if the leading-edge thrust is zero, then a complete separation has occurred. Otherwise, only partial separation exists. Now, it is known that the leading-edge thrust is related to the net upwash at the leading edge (ref. 12) so that the leading-edge boundary condition can be written as

$$V_n = a_\ell + V_{\infty n} \quad (37)$$

where $V_{\infty n}$ is given by the right-hand side of equation (9) and a_ℓ is given by (refs. 11 and 12)

$$\begin{aligned} a_\ell &= \text{total induced normalwash} - V_{\infty n} \\ &= N \sqrt{\tan^2 \Lambda_\ell + \beta^2} \left(\frac{2 c_t \cos \Lambda_\ell}{\pi \sqrt{1 - M_\infty^2 \cos^2 \Lambda_\ell}} \right)^{1/2} \end{aligned} \quad (38)$$

For a case with complete leading-edge separation, $c_t = 0$ and so is a_ℓ . Note that c_t may be zero at a portion of the leading edge and not zero at other parts, depending on such factors as leading-edge radius and thickness distributions.

Equation (37), together with the force-free conditions on all free vortex segments, is solved iteratively (ref. 11). To reduce the computing time, the total number of vortex segments used may be reduced by half during the first few iterations. In addition, to avoid numerical instability associated with

crowded vortex filaments, an option is provided to calculate the induced velocity at midpoints between two adjacent filaments and interpolate the results for the induced velocity at the filaments for the purpose of satisfying the force-free condition.

2.3.2. Effect of Leading-Edge Radius on Vortex Separation

As indicated earlier, the strength of vortex filaments is affected by the leading-edge radius. A simple, yet effective concept is needed to connect the two. In the present method, this is provided by Kulfan's assumptions (refs. 16 and 17)).

Kulfan assumed that on a slender wing the leading-edge vortex separation starts at an angle of attack (α_s) at which the leading-edge drag equals the leading-edge thrust (refs. 16 and 17). This condition has been shown to be consistent with the angle of attack at which the leading-edge laminar separation first occurs (ref. 18). To calculate α_s , consider a cambered wing. The sectional leading-edge thrust coefficient can be written as

$$c_t = K(\sin \alpha + \alpha_o)^2 \quad (39)$$

where K is a function of geometry and Mach number, and α_o is the sectional angle of zero lift. For a wing, the sectional leading-edge thrust coefficient was given in equation 27. The leading-edge singularity parameter at any α can be written as

$$C = K(\sin \alpha + \alpha_o) \quad (40)$$

Therefore, the leading-edge singularity parameter C_1 at α_s is obtained as

$$C_1 = C(\sin \alpha_s + \alpha_o)/(\sin \alpha + \alpha_o) \quad (41)$$

The starting angle of attack (α_s) of the leading-edge vortex separation can be obtained by equating the leading-edge drag to the leading-edge thrust. Using the expression for the leading-edge drag from reference 19, it is obtained that

$$\pi \frac{r_o}{c} \frac{\cos \Lambda_\ell}{(1 - M_\infty^2 \cos^2 \Lambda_\ell)^{1/2}} = \frac{\pi}{2} C^2 \frac{(\sin \alpha_s + \alpha_o)^2 (1 - M_\infty^2 \cos^2 \Lambda_\ell)^{1/2}}{(\sin \alpha + \alpha_o)^2 \cos \Lambda_\ell} \quad (42)$$

where r_o is the leading-edge radius. It follows that

$$\alpha_s = \sin^{-1} \left[\pm \frac{\sin \alpha + \alpha_o}{c} \left(2 \frac{r_o}{c} \right)^{1/2} \cos \Lambda_\ell / (1 - M_\infty^2 \cos^2 \Lambda_\ell)^{1/2} - \alpha_o \right] \quad (43)$$

With α_s calculated, the sectional thrust coefficient at $\alpha > \alpha_s$ is given by

$$c_t = (\pi/2) C_2^2 (1 - M_\infty^2 \cos^2 \Lambda_\ell)^{1/2} / \cos \Lambda_\ell \quad (44)$$

where

$$C_2 = C[\sin(\alpha - \alpha_s) + \alpha_o]/(\sin \alpha + \alpha_o) \quad (45)$$

This sectional thrust coefficient is subtracted from the full-thrust value to obtain the residual thrust which is used in equation (38).

2.3.3. Effect of Wing Thickness Distribution

Experiments show that the leading-edge vortex cores move upwards and outwards due to thickness (ref. 20). This may be due to the following reasons. Firstly, wing thickness affects the induced velocity in the flow

field. Secondly, following Kulfan (ref. 16), the flow from the lower surface has a smaller angle to turn around the leading edge to the upper surface of a thick wing. Therefore, the net centrifugal force necessary to turn the attached flow is less than that required for a thin wing. It follows that the leading-edge thrust is reduced.

To account for the induced flow produced by wing thickness, a source distribution is used with the velocity potential given by

$$\phi = -\frac{1}{4\pi} \iint_{S_w} \frac{\sigma(x', y', z') ds}{\sqrt{(x-x')^2 + \beta^2(y-y')^2 + \beta^2(z-z')^2}} \quad (46)$$

where σ is the source strength:

$$\sigma = \left(\frac{\partial\phi}{\partial n}\right)_+ - \left(\frac{\partial\phi}{\partial n}\right)_- \quad (47)$$

With the unit normal vector due to thickness given by

$$\vec{n}_t = \left[-\frac{\partial z_t}{\partial x} \vec{i} - \frac{\partial z_t}{\partial y} \vec{j} + \vec{k} \right] / \sqrt{1 + \left(\frac{\partial z_t}{\partial x}\right)^2 + \left(\frac{\partial z_t}{\partial y}\right)^2} \quad (48)$$

and

$$\vec{V}_\infty = \cos \alpha \vec{i} + \sin \alpha \vec{k},$$

the outflow velocity, $\frac{\partial\phi}{\partial n}$, can be shown to be

$$\frac{\partial\phi}{\partial n} = (\vec{V}_\infty \cdot \vec{n}_t) = \left[-\frac{\partial z_t}{\partial x} \cos \alpha + \sin \alpha \right] / \sqrt{1 + \left(\frac{\partial z_t}{\partial x}\right)^2 + \left(\frac{\partial z_t}{\partial y}\right)^2} \quad (49)$$

This outflow velocity is the one produced by the freestream. The one produced by the source distribution is to cancel this velocity component and is equal

to equation (49) with the sign reversed. It follows that the source strength can be calculated as

$$\sigma = \left[2 \left(\frac{\partial z}{\partial x} \right) \cos \alpha \right] / \sqrt{1 + \left(\frac{\partial z}{\partial x} \right)^2 + \left(\frac{\partial z}{\partial y} \right)^2} \quad (50)$$

The induced velocity produced by equation (46) is calculated through a source lattice method which is derived in Appendix A.

Experimental measurements show that on wings with asymmetric thickness distribution, the lower surface has virtually no effect on the vortex development (ref. 21). Therefore, to account for the flow turning angle at the leading edge, the angle of attack will be reduced by the upper surface nose angle δ_N (ref. 22). In other words, in equation (45) α_s is to be replaced by $(\alpha_s + \delta_N)$. The nose angle for a symmetric wedge configuration is equal to half of the included angle. For a conventional airfoil section, the slope calculated at 5% local chord position near the leading edge was used in reference 22 as the nose angle and the same value has been used in the present method as well (Fig. 6).

2.3.4. Effect of Boundary Layer Separation

By boundary layer separation it is meant that after separation there is a thick wake without a strong "organized" vortex flow, as usually present on a wing of moderate to high aspect ratio and small leading-edge sweep angles at high angles of attack. To calculate the associated complex flow field would require solving the Navier-Stokes equations with appropriate turbulent modeling. Since this is not feasible at the present time for preliminary design, a method based on utilizing nonlinear section data was developed (ref.

10). This method was based on the concept of matching the near field lift (or vorticity) with the far field value provided by the lifting surface theory.

Based on this concept, it is assumed that the effect of flow separation is to reduce the local angle of attack by $\Delta\alpha$ at a spanwise station (ref. 10). Therefore, the effective angle of attack at any spanwise section becomes

$$\alpha_e = \alpha_n - \alpha_i - \alpha_o - \Delta\alpha \quad (51)$$

where α_n is the geometric angle normal to the section which may have dihedral, α_i is the induced angle of attack, α_o is the angle of zero lift, and $\Delta\alpha$ represents a reduction in α_n to be calculated due to viscous effects. It follows that

$$c_{l(3-D)} = c_{l\alpha} \sin(\alpha_n - \alpha_i - \alpha_o - \Delta\alpha) \quad (52)$$

Assuming $c_{l\alpha} = 2\pi/(1 - M_\infty^2)^{1/2}$, equation (51) can be solved for α_i :

$$\alpha_i = \alpha_n - \sin^{-1} \left[\frac{c_{l(3-D)}}{c_{l\alpha}} \right] - \alpha_o - \Delta\alpha \quad (53)$$

Let the 2-D sectional lift coefficient evaluated at $\alpha_n - \alpha_i$ be $c_{l(2-D)}$ and let

$$f = \frac{c_{l(2-D)}}{c_{l(3-D)}} \quad (54)$$

Since $c_{l(3-D)}$ is computed with an inviscid theory, its value is usually larger than $c_{l(2-D)}$ if $\Delta\alpha = 0$. Therefore, f is usually less than 1.0. In this case, a geometric angle of attack (α') which produces the reduced lift

can be found. That is,

$$\sin \alpha' = f \sin \alpha_n$$

or,

$$\alpha' = \sin^{-1}(f \sin \alpha_n) \quad (55)$$

It follows that $\Delta\alpha$ in equation (51) becomes

$$\Delta\alpha = \alpha_n - \alpha' \quad (56)$$

The solution is obtained iteratively as follows:

1. Assume $\Delta\alpha = 0$.
2. Find α_1 from equation (53).
3. Calculate f from equation (54).
4. Determine $\Delta\alpha$ from equations (55) and (56).
5. Use $\Delta\alpha$ to reduce α in the 3-D boundary condition to determine $c_{\lambda(3-D)}$.
6. Repeat steps 2 through 5 until the successive total lift coefficients differ by less than 0.5%.

For a wing with weak or moderate vortex flow, such as that in a strake-wing configuration, iterations for vortex filaments will start only after the iterations for nonlinear section data are completed.

This method is not applicable to those configurations which are dominated by vortex flow, such as the F-106B configuration.

2.3.5. Effect of Vortex Breakdown

The effect of vortex breakdown is one of the important factors affecting the aerodynamics of high performance aircraft. Since there is no comprehensive theory to predict the breakdown location and the residual vortex strength after breakdown, a semi-empirical formula derived from a least-square analysis of available data is used in the program.

Lamar (ref. 23) observed that for delta wings, the angles of attack for vortex breakdown at the trailing edge (α_{BD}) is related to the leading-edge suction distribution (c_s). Let

$$\bar{c}_s = c c_s / \bar{c} \sin^2 \alpha \quad (57)$$

where \bar{c} is the mean aerodynamic chord (MAC). Since c_s is proportional to $\sin^2 \alpha$, it follows that \bar{c}_s is a function of planform and Mach numbers. From a least-square analysis of Wentz' data (ref. 24), it was found that α_{BD} , expressed in degrees, would fall on a single curve described as follows (Fig. 7a)

$$\alpha_{BD} = 9.195 - 23.734\bar{y}_l + 60.810\bar{y}_l^2 - 33.533\bar{y}_l^3 + 7.391\bar{y}_l^4 - 0.581\bar{y}_l^5,$$

if $\bar{y}_l < 2.5$.

$$\alpha_{BD} = 38.0, \quad \text{if } \bar{y}_l > 2.5 \quad (58)$$

where \bar{y}_l is the distance from apex to centroid of the \bar{c}_s distribution from inboard to η of $\bar{c}_{s(\max)}$ measured along the leading edge and referred to the half span. This is illustrated in Figure 7a.

The progression of the breakdown point on delta wings at $\alpha > \alpha_{BD}$ was also analyzed based on Wentz' data. Although there was considerable scatter in the experimental data (Fig. 7b), a single curve based on a least-square analysis was obtained to be

$$\begin{aligned} \Delta \bar{x} &= 0.457(\Delta\alpha) - 0.1615(\Delta\alpha)^2 + 0.0303(\Delta\alpha)^3 - 0.00237(\Delta\alpha)^4 \\ &\quad + 0.00009(\Delta\alpha)^5, \quad \text{if } \Delta\alpha < 8.0 \text{ deg.} \quad (59) \\ \Delta \bar{x} &= 0.5392 + 0.0226(\Delta\alpha), \quad \text{if } \Delta\alpha > 8.0 \text{ deg.} \end{aligned}$$

where $\Delta\alpha = \alpha - \alpha_{BD}$ and $\Delta \bar{x}$ is the nondimensional x-distance, referred to the root chord, from the trailing edge to the breakdown point.

It is known that the vortex strength after breakdown is reduced but not vanished. In the present method, the vortex strength outboard of a station where vortex breakdown occurs is multiplied by a factor k to represent the residual vortex lift. The factor k is determined again by analyzing Wentz' data and is found to be (ref. 25)

$$\begin{aligned} k &= 0.131 + 0.384\bar{y}_\ell, & \text{if } \bar{y}_\ell < 1.49 \\ k &= 0.951 - 0.208\bar{y}_\ell + 0.028\bar{y}_\ell^2, & \text{if } 1.49 < \bar{y}_\ell < 3.71 \\ k &= 0.5, & \text{if } \bar{y}_\ell > 3.72 \end{aligned} \quad (60)$$

In addition, camber (including vortex flaps) will affect α_{BD} . In the present code, it is assumed that the leading-edge vortex will burst only when it reaches the strength corresponding to a flat planform. The strength can be represented by the total leading-edge suction integrated to $\bar{c}_{s(\max)}$. If C_{sc}

and C_{sf} are these integrated values for a cambered wing and the corresponding flat wing, respectively, then

$$\frac{C_{sc}}{C_{sf}} = \frac{\sin^2 (\alpha - \bar{\alpha}_0)}{\sin^2 \alpha} \quad (61)$$

from which $\bar{\alpha}_0$ can be found. $\bar{\alpha}_0$ is to be added to α_{BD} obtained earlier for a flat wing when camber is present.

Furthermore, it was found that upper surface slopes in the spanwise direction due to thickness distribution will affect the movement of the burst point (ref. 26). To model this effect, it is assumed that the local angle of attack is changed by an amount equal to the spanwise upper surface angle; i.e., $\tan^{-1}(\partial z/\partial y)$. The new local angle of attack is used in equation (59) to determine the vortex burst point iteratively because $\partial z/\partial y$ is, in general, not a constant. This effect was found to be quite significant for a highly cambered wing, such as the F-106B configuration.

For a wing with a sideslip angle β , the angles of attack for vortex breakdown on the windward side (α_{BR}) and the leeward side (α_{BL}) are calculated as follows:

1. Calculate \bar{y}_ℓ from the symmetrical suction distribution with the leading edge sweep angles $\Lambda_\ell - \beta$ for the right wing and $\Lambda_\ell + \beta$ for the left wing.
2. Assume that the maximum vortex strength before breakdown is unchanged by sideslip. Because of increase in vortex lift on the right wing in a positive sideslip, the maximum vortex strength would be reached at a lower α (i.e., α_{BR}) than α_{BD} on the right wing. Since the vortex strength is represented by c_s which is proportional to $\sin^2 \alpha$, α_{BR}

and α_{BL} can be obtained by solving the following equation:

$$\sin^2 \alpha_{BD} = \sin^2 \alpha_{BR} + (\pm 2 \sin \beta + \tan \Lambda_\lambda \sin^2 \beta) \sin^2 \alpha_{BR} \quad (62)$$

where "-" is for α_{BL} .

The effect of yawing on vortex breakdown is similar to that due to sideslip. Since the equivalent sideslip (β_r) is variable along the leading edge, the average of β_r at a given y station and that at the tip is used to determine breakdown α . In the program, α_{BL} for the yawing motion is determined by a linear interpolation between α_{BD} and α_{BR} for sideslip.

In a rolling motion, the local angle of attack on the right wing is increased due to a positive roll. It seems that the vortex breakdown angle would be decreased. However, rolling tends to move the centroid of the vortex lift distribution outboard (i.e., to increase \bar{y}_λ). Therefore, the vortex breakdown angle is increased. In the present code, the vortex breakdown angle for the rolling motion is assumed to be equal to α_{BD} for the symmetrical loading.

2.3.6. Forebody Vortex Separation

It is well known that a fighter forebody may generate symmetric or asymmetric vortex separation at high angles of attack and zero sideslip. Asymmetric separation will produce side force, and hence, yawing moment (ref. 27). Although the vortex lattice method has been used to model the symmetrical vortex separation on a body of revolution (ref. 28), there is no three-dimensional modeling of asymmetric separation at zero sideslip available for applications in preliminary design. However, it was shown in reference 29 by a slender body theory with two discrete vortices that asymmetric vortex

separation could be obtained as the additional solution in a boundary value problem. This additional solution may generate a positive or negative side force with equal probability. This concept is now included in the present code as follows.

Calculated results from the slender body theory are valid in the near field and provide the strengths and initial locations of two forebody vortices. The locations of these forebody vortices in the wing downwash field are adjusted at the same time as the wing free vortex filaments are adjusted in position. The slender body theory will be applied at an effective angle of attack (α_e) at several stations of the forebody to include the wing upwash and body camber, if any.

Since a forebody is typically not of the circular cross section, a numerical conformal mapping is applied at computational stations to map each forebody cross section into a circular one with radius "a". The mapping function used is (ref. 30)

$$Z = \zeta + \sum_{n=1}^k \frac{A_n a^{n+1}}{\zeta^n} \frac{1}{i^{n+1}} - iC \quad (63)$$

where Z represents a complex variable in the physical plane and ζ the circle plane (see Appendix B).

The complex potential on the circle plane includes images of vortices and a source term to represent the effect of expansion of body cross sections (see Fig. 8):

$$W(\zeta) = -iV_\infty \sin \alpha_e \left(\zeta - \frac{a^2}{\zeta} \right) - V_\infty \sin \beta \left(\zeta + \frac{a^2}{\zeta} \right) + \frac{\Gamma_1}{2\pi i} \ln \frac{\zeta - \zeta_1}{\zeta - \frac{a^2}{\zeta_1}} - \frac{\Gamma_2}{2\pi i} \ln \frac{\zeta - \zeta_2}{\zeta - \frac{a^2}{\zeta_2}} + W_s(Z) \quad (64)$$

where $\bar{\zeta}_1$ and $\bar{\zeta}_2$ are complex conjugates of ζ_1 and ζ_2 , respectively. The complex velocity is given in equation (B.8) of Appendix B. The boundary conditions to be satisfied are (ref. 29):

1. At separation points, s_1 and s_2 (see Fig. 8), tangential velocities corresponding to the unknown vortex strengths are imposed.
2. The vortices are force-free.

The resulting nonlinear algebraic equations are solved simultaneously for Γ_1 , x_1 , y_1 , Γ_2 , x_2 , y_2 , where (x,y) are the vortex core coordinates in the physical plane. Typically, two pairs of realistic solutions--one symmetrical and one asymmetrical--can be obtained. The asymmetrical solution produces a side-force and hence, a yawing moment at zero sideslip. In lateral-directional motion, or with asymmetrical separation points, two branches of solutions, both asymmetrical can be obtained. Since it is not known when the second branch (which is more asymmetrical) may appear under a given flight condition, the second branch of solutions may be used to calculate the maximum possible side force and yawing moment for design purpose.

Detailed expressions for the boundary value problem in slender body theory can be found in Appendix B and reference 29.

2.4. Calculation of Aerodynamic Characteristics

The pressure distribution on lifting surfaces is calculated by applying Kutta-Joukowski's theorem. There are two types of contribution to the lifting pressure coefficients. One is from the bounded vortex elements and the other from the chordwise vortex elements. ΔC_p from the bounded elements can be written as

$$(\Delta C_p)_B = 2(u - v \tan \psi)\gamma \quad (65)$$

where u, v are the total x - and y -velocity components and ψ the element sweep angle. The lifting pressure coefficient from a chordwise vortex element has the following form:

$$(\Delta C_p)_T = 2\Gamma v \quad (66)$$

Note that the sidewash (v) is mainly produced by the free vortex filaments. The calculated ΔC_p is interpolated, if necessary, to obtain ΔC_p at integration stations and may be printed out at pre-selected locations. For more details, reference 11 should be consulted.

The calculated pressure force is assumed to be acting normal to the camber surface. This pressure force is then resolved and integrated to obtain the following sectional characteristics:

$$c_l = \frac{1}{c} \int_{x_{le}}^{x_{te}} \Delta C_p \left[\frac{\partial z}{\partial x} \sin \alpha + \cos \alpha \right] / \left[1 + \left(\frac{\partial z}{\partial x} \right)^2 + \left(\frac{\partial z}{\partial y} \right)^2 \right]^{1/2} dx \quad (67)$$

$$c_d = \frac{1}{c} \int_{x_{le}}^{x_{te}} \Delta C_p \left[-\frac{\partial z}{\partial x} \cos \alpha + \sin \alpha \right] / \left[1 + \left(\frac{\partial z}{\partial x} \right)^2 + \left(\frac{\partial z}{\partial y} \right)^2 \right]^{1/2} dx \quad (68)$$

$$c_m = -\frac{1}{c} \int_{x_{le}}^{x_{te}} \Delta C_p \left(\Delta x + \Delta z \frac{\partial z}{\partial x} \right) / \left[1 + \left(\frac{\partial z}{\partial x} \right)^2 + \left(\frac{\partial z}{\partial y} \right)^2 \right]^{1/2} dx \quad (69)$$

In an attached flow, c_d is reduced with the leading-edge thrust. The total force coefficients are calculated by spanwise integration of sectional force coefficients as

$$C_L = \frac{2}{S} \int_0^{b/2} c_l cdy \quad (70)$$

$$C_D = \frac{2}{S} \int_0^{b/2} c_d cdy \quad (71)$$

$$C_m = \frac{2}{Sc} \int_0^{b/2} c_m c^2 dy \quad (72)$$

To calculate the pressure coefficient on the fuselage, the tangential velocity component on the body surface is needed. For this purpose, the unit tangent vector on the surface will be determined first. Note that in a crossflow plane, the unit normal vector, \vec{n} , is (see Fig. 3 and equation (11))

$$\vec{n} = \frac{\vec{e}_r + \vec{e}_\theta \frac{1}{R} \frac{\partial R}{\partial \theta}}{\sqrt{1 + \left(\frac{1}{R} \frac{\partial R}{\partial \theta}\right)^2}}$$

It follows that the unit tangent vector, \vec{t} , is

$$\vec{t} = \frac{\vec{e}_r \left(\frac{1}{R} \frac{\partial R}{\partial \theta}\right) - \vec{e}_\theta}{\sqrt{1 + \left(\frac{1}{R} \frac{\partial R}{\partial \theta}\right)^2}} \quad (73)$$

With the total velocity given by equation (13), the total tangential velocity in a crossflow plane is then given by

$$v_t = \vec{V} \cdot \vec{t} \quad (74)$$

For example, in a symmetrical flight condition,

$$v_t = \left[(v_r + V_\infty \sin \alpha \cos \theta) \frac{1}{R} \frac{\partial R}{\partial \theta} - v_\theta - V_\infty \sin \alpha \sin \theta \right] / \sqrt{1 + \left(\frac{1}{R} \frac{\partial R}{\partial \theta}\right)^2} \quad (75)$$

The pressure coefficient is then (ref. 9)

$$C_{p(f)} = 1 - (1+u)^2 + M_\infty^2 u^2 + \left(\cos \alpha \frac{\partial R}{\partial x}\right)^2 + v_t^2 \quad (76)$$

The sectional normal and axial force coefficients are obtained by decomposing the pressure force into the appropriate directions as follows

$$c_n = -\frac{1}{R_{\text{ref}}} \int_{-\pi}^{\pi} C_{p(f)} \frac{\vec{\nabla F}}{|\nabla F|} \cdot \vec{k} \, ds$$

$$c_n \left(\begin{array}{c} \vec{c}_n \\ \vec{x}_n \end{array} \right) = -\frac{1}{R_{\text{ref}}} \int_{-\pi}^{\pi} C_{p(f)} \frac{\vec{\nabla F}}{|\nabla F|} \cdot \vec{k} \sqrt{1 + \left(\frac{1}{R} \frac{\partial R}{\partial \theta}\right)^2} R d\theta \quad (77)$$

$$c_A = -\frac{1}{R_{\text{ref}}} \int_{-\pi}^{\pi} C_{p(f)} \frac{\vec{\nabla F}}{|\nabla F|} \cdot \vec{i} \sqrt{1 + \left(\frac{1}{R} \frac{\partial R}{\partial \theta}\right)^2} R d\theta \quad (78)$$

Using equation (11) for $\vec{\nabla F}$ and equation (12b) for \vec{k} , it is obtained that

$$c_n = -\frac{1}{R_{\text{ref}}} \int_{-\pi}^{\pi} C_{p(f)} \frac{\cos \theta + \sin \theta \frac{1}{R} \frac{\partial R}{\partial \theta}}{\sqrt{1 + \left(\frac{1}{R} \frac{\partial R}{\partial \theta}\right)^2 + \left(\frac{\partial R}{\partial x}\right)^2}} \sqrt{1 + \left(\frac{1}{R} \frac{\partial R}{\partial \theta}\right)^2} R d\theta \quad (79)$$

$$c_A = -\frac{1}{R_{\text{ref}}} \int_{-\pi}^{\pi} C_{p(f)} \frac{\frac{\partial R}{\partial x}}{\sqrt{1 + \left(\frac{1}{R} \frac{\partial R}{\partial \theta}\right)^2 + \left(\frac{\partial R}{\partial x}\right)^2}} \sqrt{1 + \left(\frac{1}{R} \frac{\partial R}{\partial \theta}\right)^2} R d\theta \quad (80)$$

The side force coefficient can be calculated in a similar manner:

$$\begin{aligned} c_Y &= -\frac{1}{R_{\text{ref}}} \int_{-\pi}^{\pi} C_{p(f)} \frac{\vec{\nabla F}}{|\nabla F|} \cdot \vec{j} \sqrt{1 + \left(\frac{1}{R} \frac{\partial R}{\partial \theta}\right)^2} R d\theta \\ &= -\frac{1}{R_{\text{ref}}} \int_{-\pi}^{\pi} C_{p(f)} \frac{\sin \theta - \cos \theta \frac{1}{R} \frac{\partial R}{\partial \theta}}{\sqrt{1 + \left(\frac{1}{R} \frac{\partial R}{\partial \theta}\right)^2 + \left(\frac{\partial R}{\partial x}\right)^2}} \sqrt{1 + \left(\frac{1}{R} \frac{\partial R}{\partial \theta}\right)^2} R d\theta \end{aligned} \quad (81)$$

By integrating sectional coefficients along the fuselage, the total force coefficient can be obtained. For example, the normal force coefficient is

$$C_{N(f)} = \frac{1}{S} \int_{s_{f\ell}}^{x_{ft}} R_{ref} c_{n(f)} dx \quad (82)$$

The pitching moment coefficient is

$$C_{m(f)} = - \frac{1}{Sc} \int_{x_{f\ell}}^{x_{ft}} R_{ref} c_{n(f)} x dx \quad (83)$$

3. NUMERICAL RESULTS AND DISCUSSION

For the purpose of identification, the present code will be called the VORSTAB-II code in the following. In using the code, whenever the airfoil sectional data are needed, they are generated with a modified Eppler's code (ref. 33). In the following, calculated results for F/A-18, F-5, F-16XL, and F-106B configurations will be presented. All calculations are made in eight iterations to adjust the free vortex and wake positions, except for the F16XL where 10 iterations are needed. The vortex-breakdown effect is applied only at the last iteration. Results for α less than 10 deg. are all obtained with the method of suction analogy. The main emphasis is on lateral-directional aerodynamics.

An F/A-18 Configuration

This is a clean configuration without deflection of the leading-edge flap as shown in Fig. 9. On the strake, it is assumed that the aerodynamics are dominated by vortex flow, so that no section data are used. On the other hand, both vortex flows and viscous separation are assumed to exist on the wing at high angles of attack.

Longitudinal characteristics are compared with data in Figure 10. The results indicate that C_L , C_D , and C_m can be reasonably predicted. However, for α greater than 20 deg., there is some discrepancy in the predicted results. This is due to uncertainty in integrating the fuselage loading. Since the inviscid fuselage loading is significant, total lift would be over-predicted if all fuselage loading is included in the calculation. To solve this problem, the idea used in the USAF Datcom (ref. 35) is to exclude the region of separated flow from lift calculation. However, it is not known where the fuselage separation should occur. In the present code, it is arbitrarily set at a location where the sectional lift coefficient is 1.5.

Lateral-directional coefficients (C_{y_β} , C_{l_β} , C_{n_β}) for this configuration are presented in Figure 11. These characteristics are significantly influenced by free vortex positions, bursting locations and forebody vortices. The vortex system is illustrated in Figure 12. In a positive sideslip, the right leading-edge vortices are closer to the right vertical tail than the left ones to the left vertical tail. At an angle of attack of 25 deg., the strake vortices begin to burst at a position near the vertical tail (ref. 36). At the same time, the forebody vortices, although still weak, tend to push the right strake vortices towards the right vertical tail. It is a combination of these factors that generate more downloads on the right tail than on the left one to produce a negative C_{n_β} . As the angle of attack is further increased, the vortices will move upwards to reduce the interference effect. Overall, the calculated results agree well with data. It should be noted that the method of suction analogy is not capable of predicting this interference effect (ref. 9). The empirical prediction of vortex breakdown location at $\alpha = 25$ deg. has been shown to be in good agreement with water-tunnel results (ref. 36).

An F-5 Configuration

The F-5 configuration is particularly notable for its long forebody (fig. 13). The whole wing is assumed to be subject to the effects of viscous separation and vortex flow. The results for lateral-directional coefficients are presented in Figure 14. The calculated results indicate the loss of directional stability at a slightly lower angle of attack than the data shown. The more noteworthy is the effect of forebody vortices. The asymmetric forebody vortices at a positive sideslip are known to produce a positive sideforce to contribute to a position directional stability, i.e., $+C_{n\beta}$ (ref. 38). As it is shown in Figure 14, this effect of forebody vortices becomes significant at α 's above 25 deg. to produce a positive $C_{n\beta}$. Note that typically a vertical tail will not produce a positive $C_{n\beta}$ at high α 's. The increase in dihedral effect ($C_{l\beta}$) at higher α 's is mainly produced by an assumption in the code that the loading near the left wing tip is reduced in proportion to the sideslip angle because it behaves more like the wing trailing edge as the sideslip angle is increased. In the meantime, the right wing tip will have its loading increased to simulate the leading-edge effect.

An F-16XL Configuration

Data for this configuration are taken from ref. 39. It does not have camber and has an inboard sweep angle of 70 deg. and an outboard sweep of 50 deg. (Fig. 15). Because of the expected strong vortex flow, it is assumed that it is dominated by vortex flow and that no airfoil section data should be used.

The lateral-directional β -derivatives are presented in Figure 16. It is seen that $C_{l\beta}$ is overpredicted at α of 35 deg. The most difficult task in modeling this configuration is again calculating the fuselage loading. Because the strong vortex flow tends to produce a large loading on the fuselage, a separated-flow model for the fuselage would be needed for a better prediction of $C_{y\beta}$. Although the predicted $C_{n\beta}$ variation is reasonable, the calculated $C_{y\beta}$ is more erratic. In the present calculation of lateral-directional characteristics, the fuselage loading is integrated only from the nose to a station at which the sectional lift coefficient is less than 1.0 or the rate of change of sectional lift coefficients is less than 1.0.

An F-106B Configuration

The wing has a conical camber and a leading-edge sweep angle of 60 deg. (fig. 17). It is assumed to be dominated by vortex flow so that nonlinear sectional data are not used. The forebody is modeled with a distribution of vertical elliptical cross sections. The forebody is transitioned into circular cross sections in the afterbody.

A typical distribution of vortex filaments for this configuration in a positive sideslip is illustrated in Figure 18. Again, at high α 's, uncertainty in fuselage modeling in both geometric shape and loading integration causes $C_{y\beta}$ to become too negative at $\alpha = 30$ deg. (fig. 19). At $\alpha = 35$ deg., the predicted $C_{n\beta}$ is not negative enough. Again, this may be related to difficulty in fuselage modeling. As shown in this figure, $C_{l\beta}$ appears to be well predicted.

Steady roll-rate derivatives for this configuration are presented in Figures 20 and 21. The present results are quite similar to those given by

the method of suction analogy (ref. 9) Good agreement with data can be obtained before vortex breakdown. However, large discrepancy between data and theoretical results exist at high α . This is because the experiment data were obtained in forced-oscillation tests. Therefore, unsteady aerodynamic phenomena, such as vortex lag and unsteady vortex bursting, would become important. Specifically, C_{l_β} must be included in the prediction. A steady flow model, such as the present one, cannot account for such phenomena.

4. CONCLUSIONS

A steady-flow aerodynamic method was developed to calculate lateral-directional aerodynamics at high angles of attack. In the method, the edge-separated vortex flow was represented by free vortex filaments and viscous separation effect was accounted for by using nonlinear section data. Forebody vortex separation was calculated with a slender body theory at an effective angle of attack which was given by the lifting surface theory. Calculated results for four configurations were compared with available wind-tunnel data. Reasonable agreement could be obtained for sideslip derivatives. Discrepancy in C_{y_β} was attributable to inaccurate fuselage modeling. It was also clear that dynamic stability coefficients at high angles of attack could not be accurately calculated with a steady flow theory.

REFERENCES

- [1] Magnus, A. E.; and Epton, E. M., "PAN AIR--A Computer Program for Predicting Subsonic or Supersonic Linear Potential Flows about Arbitrary Configurations Using a Higher Order Panel Method; Volume I: Theory Document," NASA CR-3251, April 1980.
- [2] Carmichael, R. L.; and Erickson, L. L., "PAN AIR--A Higher Order Panel Method for Predicting Subsonic or Supersonic Linear Potential Flows about Arbitrary Configurations," AIAA Paper 81-1255, June 1981.
- [3] Johnson, F. T.; Tinoco, E. N.; Lu, P.; and Upton, M. A., "Three-Dimensional Flow over Wings with Leading-Edge Vortex Separation," AIAA Journal, Vol. 18, April 1980, pp. 367-380.
- [4] Maskew, B., "Prediction of Subsonic Aerodynamic Characteristics: A Case for Low-Order Panel Methods," Journal of Aircraft, Vol. 19, February 1982, pp. 157-163.
- [5] Maskew, B.; and Rao, B. M., "Calculation of Vortex Flows on Complex Configurations," ICAS-82-6.2.3, 1982.
- [6] Dusto, A. R., et al., "A Method for Predicting the Stability Characteristics of Control Configured Vehicles," AFFDL-TR-74-91, November 1974.

- [7] De Hart, J. H.; Gilchrist, I. J.; and Jenkins, J. E., "Development of a Stability and Control Data Prediction Capability Using an Advanced Aerodynamic Paneling Program," presented at the National Aerospace and Electronics Conference, Dayton, Ohio, May 20, 1987.
- [8] Lan, C. E., "VORSTAB--A Computer Program for Calculating Lateral-Directional Stability Derivatives with Vortex Flow Effect," NASA CR-172501, January 1985.
- [9] Tseng, J. B.; and Lan, C. E., "Calculation of Aerodynamic Characteristics of Airplane Configurations at High Angles of Attack," NASA CR-4182, October 1988.
- [10] Lan, C. E., "Theoretical Prediction of Wing Rocking," AGARD CP-386, 1985.
- [11] Mehrotra, S. C.; and Lan, C. E., "A Theoretical Investigation of the Aerodynamics of Low-Aspect-Ratio Wings with Partial Leading-Edge Separation," NASA CR-145304, January 1978.
- [12] Lan, C. E., "A Quasi-Vortex-Lattice Method in Thin Wing Theory," Journal of Aircraft," Vol. 11, September 1974, pp. 518-527.
- [13] Lan, C. E. and Chang, J. F., "Calculation of Vortex Lift Effect for Cambered Wings by the Suction Analogy," NASA CR-3449, July 1981.

- [14] Ward, G. N., "Linearized Theory of Steady High-Speed Flow," Cambridge University Press, 1955.
- [15] Lan, C. E., "Calculation of Lateral-Directional Stability Derivatives for Wing-Body Combinations with and without Jet-Interaction Effects," NASA CR-145251, August 1977.
- [16] Kulfan, R. M., "Wing Airfoil Shape Effects on the Development of Leading-Edge Vortices," AIAA Paper 79-1675, 1979.
- [17] Kulfan, R. M., "Wing Geometry Effects on Leading-Edge Vortices," AIAA Paper 79-1872, 1979.
- [18] Lan, C. E.; and Su, I., "Effect of a Round Airfoil Nose on Leading-Edge Suction," Journal of Aircraft, Vol. 24, July 1987, pp. 472-474.
- [19] Robinson, A.; and Laurmann, J. A., "Wing Theory," Cambridge University Press, 1956.
- [20] Smith, J.H.B., "Calculations of the Flow over Thick, Conical, Slender Wings with Leading-Edge Separation," British ARC R&M 3694, March 1971.
- [21] Squire, L. C., "Some Effects of Thickness on the Longitudinal Characteristics of Sharp-Edged Delta Wings at Low-Speeds," The Aeronautical Quarterly, Vol. 72, February 1968, pp. 151-155.

- [22] Hsing, C. C.; and Lan, C. E., "Design and Analysis of Vortex Flaps with and without Thickness Effect," CRINC-FRL-637-1, University of Kansas Center for Research, Inc., January 1986.
- [23] Lamar, J. E., "Recent Studies of Subsonic Vortex Lift Including Parameters Affecting Stable Leading-Edge Vortex Flow," Journal of Aircraft, Vol. 14, December 1977, pp. 1205-1211.
- [24] Wentz, W. W., Jr., "Wind Tunnel Investigation of Vortex Breakdown on Slender Sharp-Edged Wings," NASA CR-98737, 1969.
- [25] Lan, C. E.; and Hsu, C. H., "Effects of Vortex Breakdown on Longitudinal and Lateral-Directional Aerodynamics of Slender Wings by the Suction Analogy," AIAA Paper 82-1385, 1982.
- [26] Earnshaw, P. B., "Measurement of the Effects of Thickness on Vortex Breakdown Position on a Series of Sharp-Edged Delta Wings," British ARC C.P. No. 1018, 1968.
- [27] Chapman, G. T.; Keener, E. R.; and Malcolm, G. N., "Asymmetric Aerodynamic Forces on Aircraft Forebodies at High Angles of Attack - Some Design Guides," AGARD CP-199, 1975.
- [28] Almosnino, P.; and Rom, J., "Calculation of Symmetric Vortex Separation Affecting Subsonic Bodies at High Incidence," AIAA Journal, Vol. 21, March 1983, pp. 398-406.

- [29] Chin, S. and Lan, C. E., "Calculation of Symmetric and Asymmetric Vortex Separation on Cones and Tangent Ogives Based on Discrete Vortex Models," NASA CR-4122, February 1988.
- [30] Skulsky, R. S., "A Conformal Mapping Method to Predict Low-Speed Aerodynamic Characteristics of Arbitrary Slender Re-Entry Shapes," Journal of Spacecraft and Rockets, Vol. 3, February 1966, pp. 247-253.
- [31] Mendenhall, M. R.; Spangler, S. B.; and Perkins, S. C. Jr., "Vortex Shedding from Circular and Noncircular Bodies at High Angles of Attack," AIAA Paper 79-0026, January 1979.
- [32] Ward, G. N., "Supersonic Flow Past Slender Pointed Bodies," Quarterly Journal of Mechanics and Applied Mathematics, Vol. II, Part I, 1949, pp. 75-97.
- [33] Eppler, R.; and Somers, D. M., "A Computer Program for the Design and Analysis of Low-Speed Airfoils," NASA TM-80210, 1980.
- [34] Lutze, F. H., "Curved Flow Wind Tunnel Test of F-18 Aircraft," VPI-Aero-108, April 1980.
- [35] Finck, R. D., et al., "USAF Stability and Control Datcom," U. S. Air Force Flight Dynamics Laboratory, Wright-Patterson Air Force Base, Ohio, October 1960 (Revised April 1978).

- [36] Lan, C. E.; and Lee, I. G., "Investigation of Empennage Buffeting," NASA CR 179426, January 1987.
- [37] Grafton, S. B.; Chambers, J. R.; and Coe, P. L., Jr., "Wind-Tunnel Free-Flight Investigation of a Model of a Spin-Resistant Fighter Configuration," NASA TN D-7716, 1974.
- [38] Skow, A. M.; and Erickson, G. E., "Modern Fighter Aircraft Design for High Angle-of-Attack Maneuvering," AGARD LS-121, 1982.
- [39] Grafton, S. B., "Low-Speed Wind-Tunnel Study of the High Angle-of-Attack Stability and Control Characteristics of a Cranked-Arrow-Wing Fighter Configuration," NASA TM-85776, May 1984.
- [40] Yip, L. P., "Wind-Tunnel Free-Flight Investigation of a 0.15-Scale Model of the F-106B Airplane with Vortex Flaps, NASA TP-2700, 1987.

APPENDIX A

A SURFACE SOURCE LATTICE METHOD

Assume that the continuous source distribution is reduced to a finite sum of discrete source element contributions. These source elements occupy the same locations as the vortex lattices. A source element is defined by its inboard endpoint coordinates (x_1, y_1, z_1) and outboard endpoint coordinates (x_2, y_2, z_2) . An integration parameter τ , representing fraction of the element, can be defined such that

$$\begin{aligned}
 x' - x &= x_1 - x + \tau(x_2 - x_1) \\
 y' - y &= y_1 - y + \tau(y_2 - y_1) \\
 z' - z &= z_1 - z + \tau(z_2 - z_1)
 \end{aligned}
 \tag{A.1}$$

Therefore, the denominator in the integrand of equation (46) can be written as

$$\begin{aligned}
 (x' - x)^2 + \beta^2 (y' - y)^2 + \beta^2 (z' - z)^2 &= \tau^2 [(x_2 - x_1)^2 + \beta^2 (y_2 - y_1)^2 \\
 &+ \beta^2 (z_2 - z_1)^2] + 2\tau [(x_1 - x)(x_2 - x_1) + \beta^2 (y_1 - y)(y_2 - y_1) \\
 &+ \beta^2 (z_1 - z)(z_2 - z_1)] + (x_1 - x)^2 + \beta^2 (y_1 - y)^2 + \beta^2 (z_1 - z)^2 \\
 &= \tau^2 A + \tau B + C
 \end{aligned}$$

where

$$A = (x_2 - x_1)^2 + \beta^2 (y_2 - y_1)^2 + \beta^2 (z_2 - z_1)^2 \quad (\text{A.2a})$$

$$B = 2[(x_1 - x)(x_2 - x_1) + \beta^2 (y_1 - y)(y_2 - y_1) + \beta^2 (z_1 - z)(z_2 - z_1)] \quad (\text{A.2b})$$

$$C = (x_1 - x)^2 + \beta^2 (y_1 - y)^2 + \beta^2 (z_1 - z)^2 \quad (\text{A.2c})$$

It follows that equation (46) can be reduced to a sum of quantities of the following form:

$$\begin{aligned} \Delta\phi &= -\frac{\sigma\Delta\ell}{4\pi} \int_0^1 \frac{d\tau}{\sqrt{A\tau^2 + B\tau + C}} \\ &= -\frac{\sigma\Delta\ell}{4\pi} \frac{1}{\sqrt{A}} \{ \ln[2A + B + 2\sqrt{A}\sqrt{A + B + C}] - \ln[B + 2\sqrt{AC}] \} \\ \Delta\ell &= \sqrt{(x_2 - x_1)^2 + (y_2 - y_1)^2 + (z_2 - z_1)^2} \end{aligned} \quad (\text{A.3})$$

By differentiation, the following induced velocity components can be obtained:

$$\frac{\partial\Delta\phi}{\partial x} = \frac{\sigma\Delta\ell}{2\pi\sqrt{A}} \left\{ \frac{x_2 - x_1 + 2\sqrt{A} \frac{x_2 - x_1}{\sqrt{A + B + C}}}{2A + B + 2\sqrt{A}\sqrt{A + B + C}} - \frac{x_2 - x_1 + 2\sqrt{\frac{A}{C}}(x_1 - x)}{B + 2\sqrt{AC}} \right\} \quad (\text{A.4})$$

$$\frac{\partial\Delta\phi}{\partial y} = \frac{\sigma\Delta\ell\beta^2}{2\pi\sqrt{A}} \left\{ \frac{y_2 - y_1 + 2\sqrt{A} \frac{y_2 - y_1}{\sqrt{A + B + C}}}{2A + B + 2\sqrt{A}\sqrt{A + B + C}} - \frac{y_2 - y_1 + 2\sqrt{\frac{A}{C}}(y_1 - y)}{B + 2\sqrt{AC}} \right\} \quad (\text{A.5})$$

$$\frac{\partial\Delta\phi}{\partial z} = \frac{\sigma\Delta\ell\beta^2}{2\pi\sqrt{A}} \left\{ \frac{z_2 - z_1 + 2\sqrt{A} \frac{z_2 - z_1}{\sqrt{A + B + C}}}{2A + B + 2\sqrt{A}\sqrt{A + B + C}} - \frac{z_2 - z_1 + 2\sqrt{\frac{A}{C}}(z - \bar{z})}{B + 2\sqrt{AC}} \right\} \quad (\text{A.6})$$

APPENDIX B

CALCULATION OF FOREBODY FLOW FIELD IN THE CROSSFLOW PLANE

By slender body theory, aerodynamic characteristics of a forebody with vortex separation can be calculated in the crossflow plane. The body cross section is first mapped conformally to a circle of radius "a." The complex potential on the circle plane can be easily constructed. The total force coefficients can be obtained by contour integration. These are summarized in the following.

B.1 Conformal Mapping

In reference 30, a formula for mapping an arbitrary polygon symmetrical about the real axis to a circle of radius "a" is given:

$$Z_1 = \zeta_1 + \sum_{n=1}^k \frac{A_n a^{n+1}}{\zeta_1^n} + C \quad (\text{B.1})$$

where C is a constant used to adjust the location of the center. Since the cross section of a forebody is usually symmetrical about the vertical axis, a rotation by $\pi/2$ is needed (see Fig. B.1):

$$\begin{aligned} \zeta_1 &= i\zeta \\ Z_1 &= iZ \end{aligned} \quad (\text{B.2})$$

It follows that equation (B.1) becomes

$$Z = \zeta + \sum_{n=1}^k \frac{A_n a^{n+1}}{\zeta^n} \frac{1}{i^{n+1}} - iC \quad (\text{B.3})$$

The derivative $dZ/d\zeta$ is needed in mapping of flow nets:

$$\frac{dZ}{d\zeta} = 1 - \sum_{n=1}^k A_n \frac{a^{n+1}}{\zeta^{n+1}} \frac{1}{1} = 1 - \sum_{n=1}^k \frac{nA_n}{\zeta^{*n+1}} \frac{1}{i^{n+1}} \quad (\text{B.4})$$

where

$$\zeta^* = \zeta/a \quad (\text{B.5})$$

For an elliptic cross section, with a_1 and a_2 as major and minor axes, an analytical form of the mapping function is

$$Z = \zeta + \frac{a_1^2 - a_2^2}{4} \frac{1}{\zeta} \quad (\text{B.6})$$

Comparing with equation (B.3), it can be shown that

$$A_1 = - \frac{a_1^2 - a_2^2}{4a^2}$$

$$a = \frac{a_1 + a_2}{2}$$

$$A_n = 0, \quad n=2,3,\dots$$

B.2 Boundary Conditions with Vortex Separation

The complex potential can be written as

$$W(\zeta) = -iV_\infty \sin \alpha \left(\zeta - \frac{a^2}{\zeta} \right) - V_\infty \sin \beta \left(\zeta + \frac{a^2}{\zeta} \right) + \frac{\Gamma_1}{2\pi i} \ln \frac{\zeta - \zeta_1}{\zeta - \frac{a^2}{\zeta_1}} - \frac{\Gamma_2}{2\pi i} \ln \frac{\zeta - \zeta_2}{\zeta - \frac{a^2}{\zeta_2}} + W_s(z) \quad (\text{B.7})$$

The complex velocity is given by

$$\begin{aligned} \frac{1}{V_{\infty} \sin \alpha} \frac{dW}{d\zeta} = & -i\left(1 + \frac{1}{\zeta^{*2}}\right) - \frac{\sin \beta}{\sin \alpha} \left(1 - \frac{1}{\zeta^{*2}}\right) - i\gamma_1 \left[\frac{1}{\zeta - \zeta_1} - \frac{1}{\zeta - \frac{1}{\zeta_1^*}}\right] \\ & + i\gamma_2 \left[\frac{1}{\zeta - \zeta_2} - \frac{1}{\zeta - \frac{1}{\zeta_2^*}}\right] + \frac{1}{V_{\infty} \sin \alpha} \frac{dW_s}{d\zeta} \end{aligned} \quad (\text{B.8})$$

where

$$\gamma_1 = \frac{\Gamma_1}{2\pi V_{\infty} a \sin \alpha} \quad (\text{B.9a})$$

$$\gamma_2 = \frac{\Gamma_2}{2\pi V_{\infty} a \sin \alpha} \quad (\text{B.9b})$$

In equation (B.8), the source term W_s is to simulate the flow field due to change in body cross sections in the x-direction. This source flow must satisfy the following condition:

$$\frac{\partial \phi_s}{\partial r} = V_{\infty} \cos \alpha \frac{dR}{dx} \quad (\text{B.10})$$

In a crossflow plane, the source flow can be simulated by

$$\phi_s = C_1(x, \theta) \ln r \quad (\text{B.11})$$

where C_1 is regarded as a function of θ because of $R(x, \theta)$. Therefore,

$$C_1(x, \theta) = (V_{\infty} \cos \alpha) R \frac{dR}{dx} \quad (\text{B.12})$$

The induced velocity due to the source flow is computed from

$$\frac{\partial \phi_s}{\partial r} = \frac{C_1(x, \theta)}{r} = \frac{(V_\infty \cos \alpha)R}{r} \frac{dR}{dx} \quad (\text{B.13})$$

Note that on the body surface, $r = R$. In addition, for a flat surface, such as a delta wing, the limiting form of equation (B.13) at the leading edge would be

$$\frac{\partial \phi_s}{\partial y} = V_\infty \cos \alpha \frac{dy}{dx} = V_\infty \cos \alpha \tan \delta_x \quad (\text{B.14})$$

where δ_x is the half apex angle of the delta wing. The velocity given by equation (B.14) is used in setting up the conditions at the separation points which are sharp-edged, such as on a delta wing or a chine cross section.

The separation locations are calculated with Stratford's criteria in the same way as used in reference 31, based on the velocity distribution computed in the three-dimensional flow model, including wing effect. At the separation points and the vortex locations, the following conditions must be satisfied.

1. Conditions at Separation Points

On a smooth surface, the mean tangential velocity (V_{t_m}) at the separation points in the physical plane is equal to the convection velocity of vortex in the shear layer after boundary layer separation (ref. 29). It is taken to be (referring to eqns. (3) and (7a) of ref. 29)

$$\begin{aligned} V_{t_m} &= \frac{2f}{\sqrt{K}} \left(\frac{V_\infty \cos \alpha}{2} \frac{\partial \Gamma}{\partial x} \right)^{1/2} = \frac{2fV_\infty \sin \alpha}{\sqrt{K}} \left[\frac{\cos \alpha}{2\pi V_\infty \sin^2 \alpha} \frac{\pi \Delta \Gamma}{\Delta x} \right]^{1/2} \\ &= \frac{2fV_\infty \sin \alpha}{\sqrt{K}} \left[\frac{\pi}{\tan \alpha} \frac{\Delta(\gamma a)}{\Delta x} \right]^{1/2} \end{aligned} \quad (\text{B.15})$$

In equation (B.15), K is taken to be 0.6 to account empirically for secondary separation which reduces the strength of the primary vortex when only the latter is used in the model. f is taken to be 0.61 to account for the vortex convection speed in a shear layer (ref. 29). This tangential velocity (V_{t_m}) should be equated to the total tangential velocity calculated in the flow model:

$$V_{t_m} = - \operatorname{Im} \left\{ e^{i\theta_k} \frac{dW}{dZ} \right\}$$

or

$$\frac{V_{t_m}}{V_\infty \sin \alpha} = - \operatorname{Im} \left\{ e^{i\theta_k} \frac{1}{V_\infty \sin \alpha} \frac{dW}{d\zeta} \frac{d\zeta}{dZ} \right\} \text{ at } Z = Z_{\text{sep}} \quad (\text{B.16})$$

where θ_k represents a tangent angle and is defined in Figure B.2, and Im stands for the imaginary part. Using equation (B.8), equation (B.16) can be rewritten as

$$\begin{aligned} \frac{V_{t_m}}{V_\infty \sin \alpha} = & - \operatorname{Im} \left\{ \frac{e^{i\theta_k}}{e^{i\theta_k^*}} \frac{d\zeta}{dZ} \left[-i(e^{i\theta_k^*} + e^{-i\theta_k^*}) - \frac{\sin \beta}{\sin \alpha} (e^{i\theta_k^*} - e^{-i\theta_k^*}) \right] \right. \\ & - i\gamma_1 \frac{\zeta_1^* \bar{\zeta}_1^* - 1}{(e^{i\theta_k^* - \zeta_1^*})(\bar{\zeta}_1^* - e^{-i\theta_k^*})} + i\gamma_2 \frac{\zeta_2^* \bar{\zeta}_2^* - 1}{(e^{i\theta_k^* - \zeta_2^*})(\bar{\zeta}_2^* - e^{-i\theta_k^*})} \\ & \left. + \frac{e^{i\theta_k}}{V_\infty \sin \alpha} \frac{dW_{s_1}}{dZ} \right\} \text{ at } Z_{\text{sep}} \quad (\text{B.17}) \end{aligned}$$

where θ_k^* is θ_k in the circle plane.

When Z_{sep} is a sharp edge so that the mapping is singular, $(dW/d\zeta)(d\zeta/dZ)$ must be first reduced by L'Hospital's rule. The resulting velocity will consist of a tangential and a normal component. The tangential

component is used in equation (B.16), but the normal component must be set to zero. This introduces one extra equation. In this case, f/\sqrt{K} in V_{t_m} must be regarded as unknown to result in a determinate set of equations.

2. Force-Free Conditions

The separated vortex should be force-free, or based on Kutta-Joukowski's theorem,

$$F_v = -i\rho\Gamma_v \left[\lim_{Z \rightarrow Z_v} \left(\frac{dW}{dz} - \frac{\Gamma_v}{2\pi i} \frac{1}{Z - Z_v} \right) - \frac{dZ_v}{dt} \right] = 0 \quad (B.18)$$

where Γ_v and Z_v may be taken to be Γ_1, Z_1 or Γ_2 and Z_2 . Replacing dt by $dx/V_\infty \cos \alpha$ and considering $\bar{F}_v = 0$, it is obtained for the right-side vortex that

$$\lim_{Z \rightarrow Z_1} \left\{ \frac{dW}{d\zeta} \frac{d\zeta}{dZ} - \frac{\Gamma_1}{2\pi i} \frac{1}{Z - Z_1} \right\} = V_\infty \cos \alpha \frac{d\bar{Z}_1}{dx} \quad (B.19)$$

Using the complex potential in equation (B.8), equation (B.19) can be reduced to

$$\begin{aligned} \frac{d\zeta}{dZ} \Big|_{Z=Z} & \left[-i \left(1 + \frac{1}{\zeta_1^{*2}} \right) - \frac{\sin \beta}{\sin \alpha} \left(1 - \frac{1}{\zeta_1^{*2}} \right) + i\gamma_1 \frac{\zeta_1^{-*}}{\zeta_1^{*-} \zeta_1^{-1}} \right. \\ & \left. + i\gamma_2 \left(\frac{1}{\zeta_1^{*-} \zeta_2^{*-}} - \frac{\zeta_2^{-*}}{\zeta_1 \zeta_2^{-1}} \right) + i\gamma_1 \lim_{Z \rightarrow Z_1} \left(\frac{dZ/d\zeta}{\zeta - \zeta_1} - \frac{1}{\zeta \zeta_1} \right) \right] \\ & + \frac{1}{V_\infty \sin \alpha} \frac{dW_s}{dz} \Big|_{Z=Z_1} - \frac{\cos \alpha}{\sin \alpha} \frac{d\bar{Z}_1}{dx} = 0 \end{aligned} \quad (B.20)$$

The same consideration applies to the left-side vortex.

For a body with a smooth surface, there are two equations representing the separation condition and four equations (one being the real and the other

imaginary part of equation (B.20)) from the force-free conditions. These six equations are to be solved for $\gamma_1, y_1, z_1, \gamma_2, y_2,$ and z_2 . These equations are highly nonlinear and they are solved by a modified Newton iterative method (ref. 29). Typically, a symmetric vortex solution can be obtained from any initial input data. To search for any additional solutions, a method of function deflation to remove the symmetric vortex solution is used to avoid convergence to the same symmetric solution again (ref. 29). The additional solution show asymmetric vortex locations and strengths.

B.3 Force Coefficients by Momentum Theory

With the vortex locations and strengths determined, the complex potential may be used to calculate the velocity on the body surface, and hence the pressure distribution. The latter may be integrated to obtain the force components. Since the force components are of primary interest in the present applications, an alternate method to calculate them is to apply the momentum equation. Based on Ward (ref. 32), the lateral force based on slender body theory is given by

$$\frac{F}{(\frac{1}{2})\rho V_\infty^2 S_{\text{ref}}} = \frac{1}{S_{\text{ref}}} \left\{ -2i \oint \frac{W}{V_\infty} dZ - 2i S_B (\sin \alpha - i \sin \beta) \right\} \quad (\text{B.21})$$

where S_B is the base area. The contour integral in equation (B.21) can be enlarged so that both $W(\zeta)$ and $dZ/d\zeta$ can be expanded for large ζ . Using equations (B.4) and (B.7), it can be shown for large ζ that

$$\begin{aligned}
W(\zeta) \frac{dZ}{d\zeta} \approx & -iV_{\infty} \sin \alpha \left(\zeta - \frac{a^2}{\zeta} \right) - V_{\infty} \sin \beta \left(\zeta + \frac{a^2}{\zeta} \right) + \frac{\Gamma_1}{2\pi i} \left[\frac{a^2}{\zeta \zeta_1} + \frac{1}{2} \left(\frac{a^2}{\zeta \zeta_1} \right)^2 \right. \\
& \left. - \frac{\zeta_1}{\zeta} - \frac{1}{2} \left(\frac{\zeta_1}{\zeta} \right)^2 \right] - \frac{\Gamma_2}{2\pi i} \left[\frac{a^2}{\zeta \zeta_2} + \frac{1}{2} \left(\frac{a^2}{\zeta \zeta_2} \right)^2 - \frac{\zeta_2}{\zeta} - \frac{1}{2} \left(\frac{\zeta_2}{\zeta} \right)^2 \right] \\
& + A_1 a^2 \left\{ -iV_{\infty} \sin \alpha \left(\frac{1}{\zeta} - \frac{a^2}{\zeta^3} \right) - V_{\infty} \sin \beta \left(\frac{1}{\zeta} + \frac{a^2}{\zeta^3} \right) + \dots \right\} \quad (B.22)
\end{aligned}$$

The contour integral can therefore be calculated by residue theorem as

$$\begin{aligned}
\oint \frac{W}{V_{\infty}} \frac{dZ}{d\zeta} d\zeta &= 2\pi i \left[-i \sin \alpha (-a^2) - \sin \beta (a^2) + \frac{\Gamma_1}{2\pi i V_{\infty}} \left(\frac{a^2}{\zeta_1} - \zeta_1 \right) \right. \\
&\quad \left. - \frac{\Gamma_2}{2\pi i V_{\infty}} \left(\frac{a^2}{\zeta_2} - \zeta_2 \right) + A_1 a^2 (-i \sin \alpha - \sin \beta) \right] \\
&= -2\pi a^2 \sin \alpha \left[1 - A_1 + i(1 + A_1) \frac{\sin \beta}{\sin \alpha} + \gamma_1 \left(\zeta_1^* - \frac{1}{\zeta_1^*} \right) - \gamma_2 \left(\zeta_2^* - \frac{1}{\zeta_2^*} \right) \right] \quad (B.23)
\end{aligned}$$

Using equation (B.21), the force coefficients can be obtained:

$$\begin{aligned}
c_Y + ic_N &= \frac{F}{\left(\frac{1}{2} \right) \rho V_{\infty}^2 S_{\text{ref}}} = \frac{i4\pi a^2 \sin \alpha}{S_{\text{ref}}} \left[1 - A_1 + i(1 + A_1) \frac{\sin \beta}{\sin \alpha} \right. \\
&\quad \left. + \gamma_1 \left(\zeta_1^* - \frac{1}{\zeta_1^*} \right) - \gamma_2 \left(\zeta_2^* - \frac{1}{\zeta_2^*} \right) \right] - 2i(\sin \alpha - i \sin \beta) \frac{S_B}{S_{\text{ref}}}
\end{aligned}$$

Since

$$\zeta_1^* = \xi_1^* + i\eta_1^*$$

$$\zeta_2^* = \xi_2^* + i\eta_2^*$$

the force coefficients become

$$c_Y = \frac{4\pi a^2 \sin \alpha}{S_{\text{ref}}} \left[- (1 + A_1) \frac{\sin \beta}{\sin \alpha} - \gamma_1 \eta_1^* \left(1 - \frac{1}{\xi_1^* + \eta_1^*} \right) \right. \\ \left. + \gamma_2 \eta_2^* \left(1 - \frac{1}{\xi_2^* + \eta_2^*} \right) \right] - 2 \sin \beta \frac{S_B}{S_{\text{ref}}} \quad (\text{B.24})$$

$$c_N = \frac{4\pi a^2 \sin \alpha}{S_{\text{ref}}} \left[1 - A_1 + \gamma_1 \xi_1^* \left(1 - \frac{1}{\xi_1^* + \eta_1^*} \right) \right. \\ \left. - \gamma_2 \eta_2^* \left(1 - \frac{1}{\xi_2^* + \eta_2^*} \right) \right] - 2 \sin \alpha \frac{S_B}{S_{\text{ref}}} \quad (\text{B.25})$$

Figure B.1. Sequence of Transformations.

Figure B.2 Velocity Components at a Separation Point S_1 .

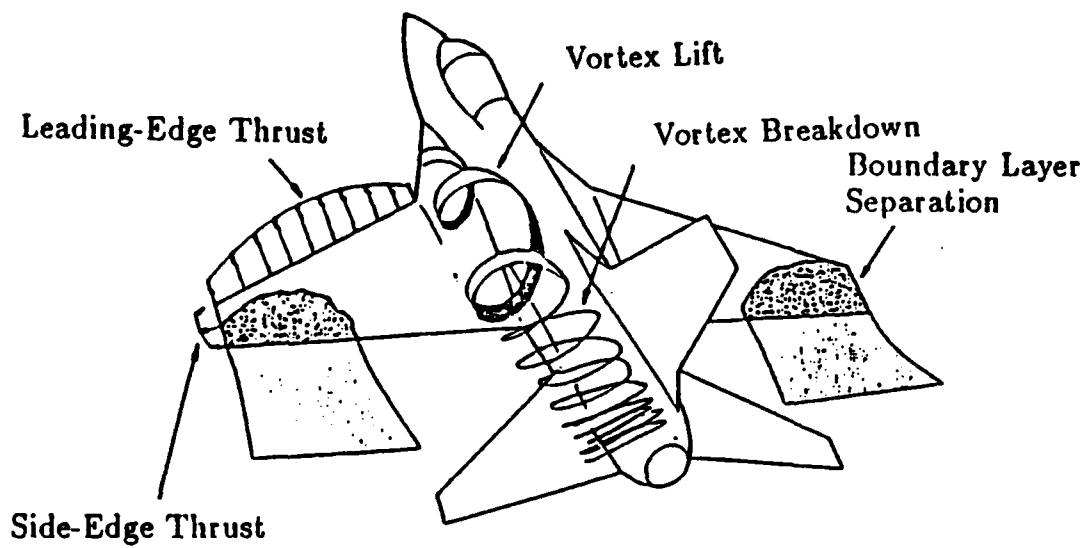


Figure 1. Illustration of Flow Features Predicted in the Present Method

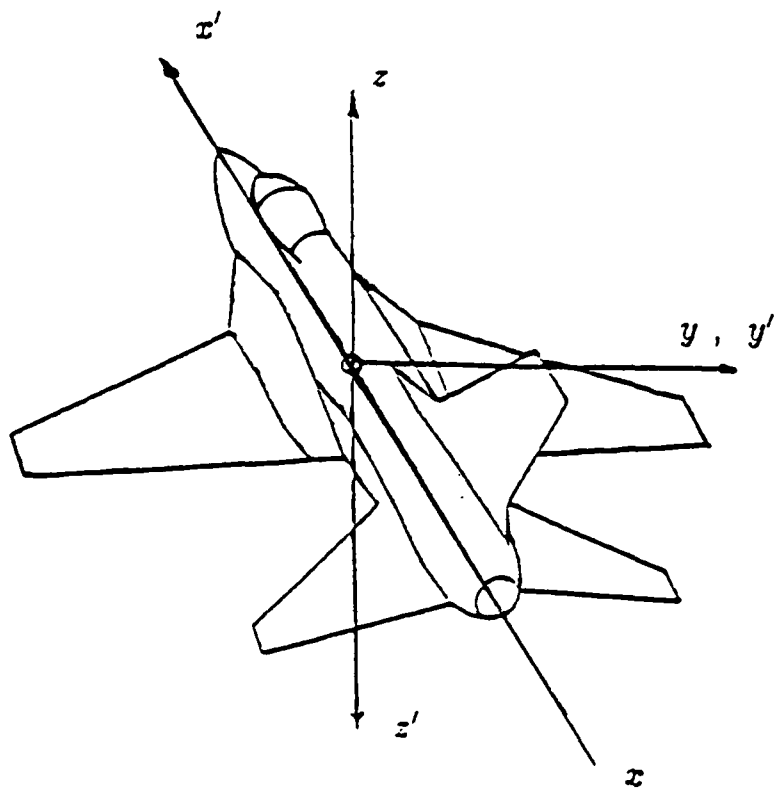


Figure 2. Definition of Airplane Coordinate Systems

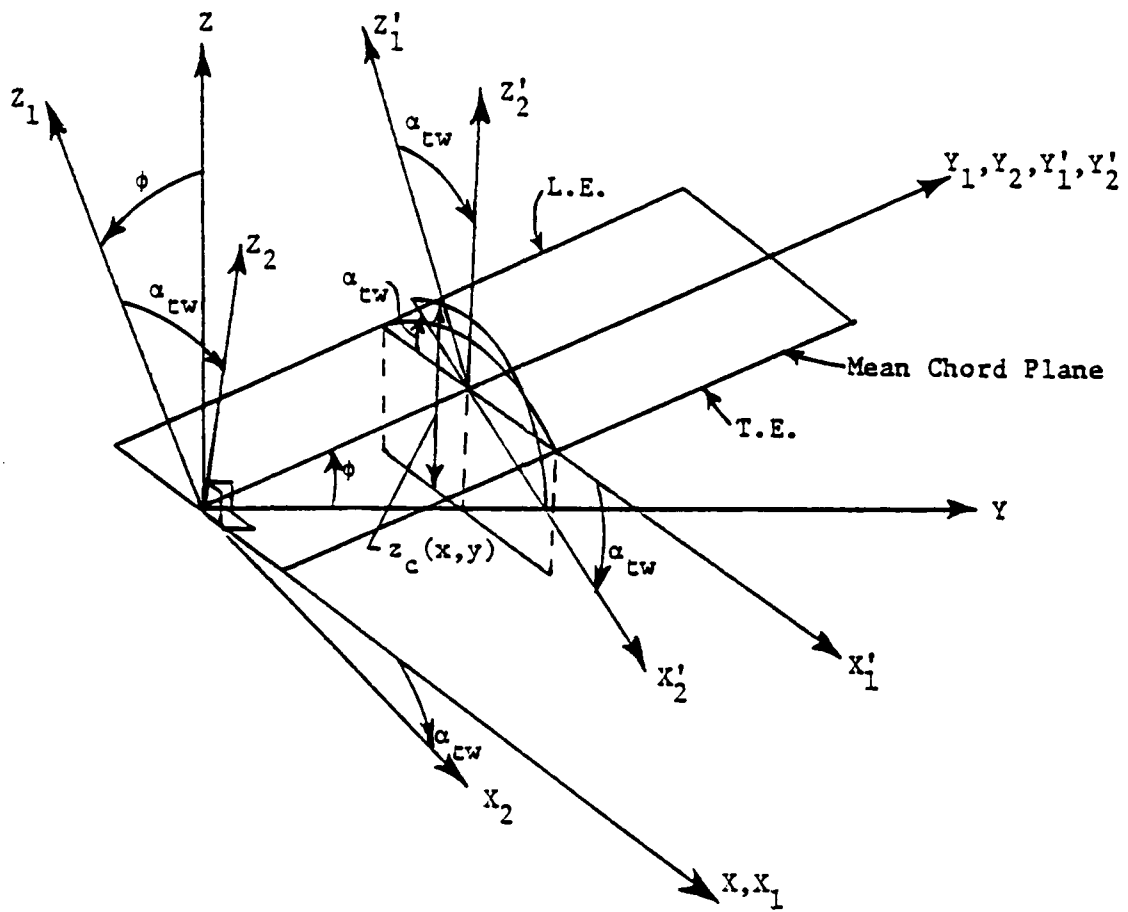


Figure 3. Definition of Variables Defining a Nonplanar Wing Surface (Ref. 13)

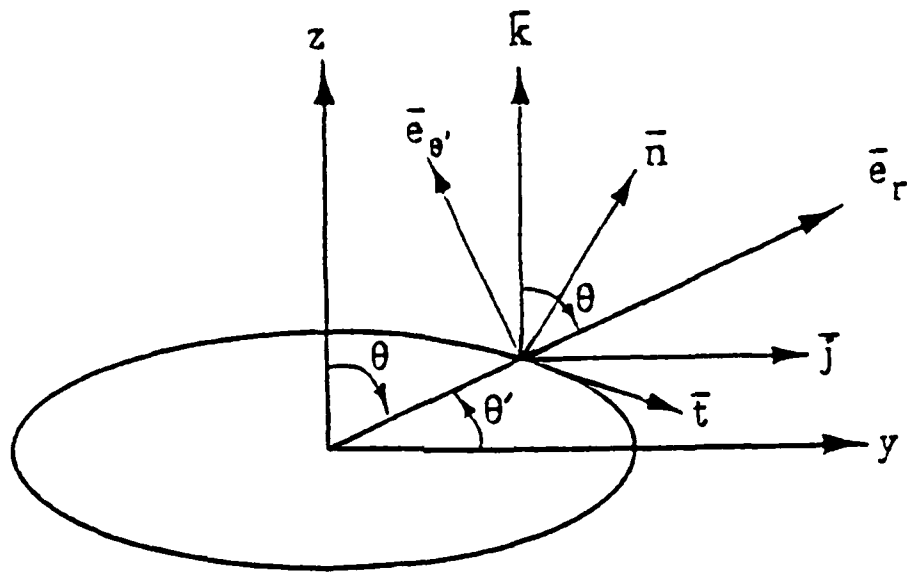


Figure 4 Fuselage Cylindrical Coordinate System

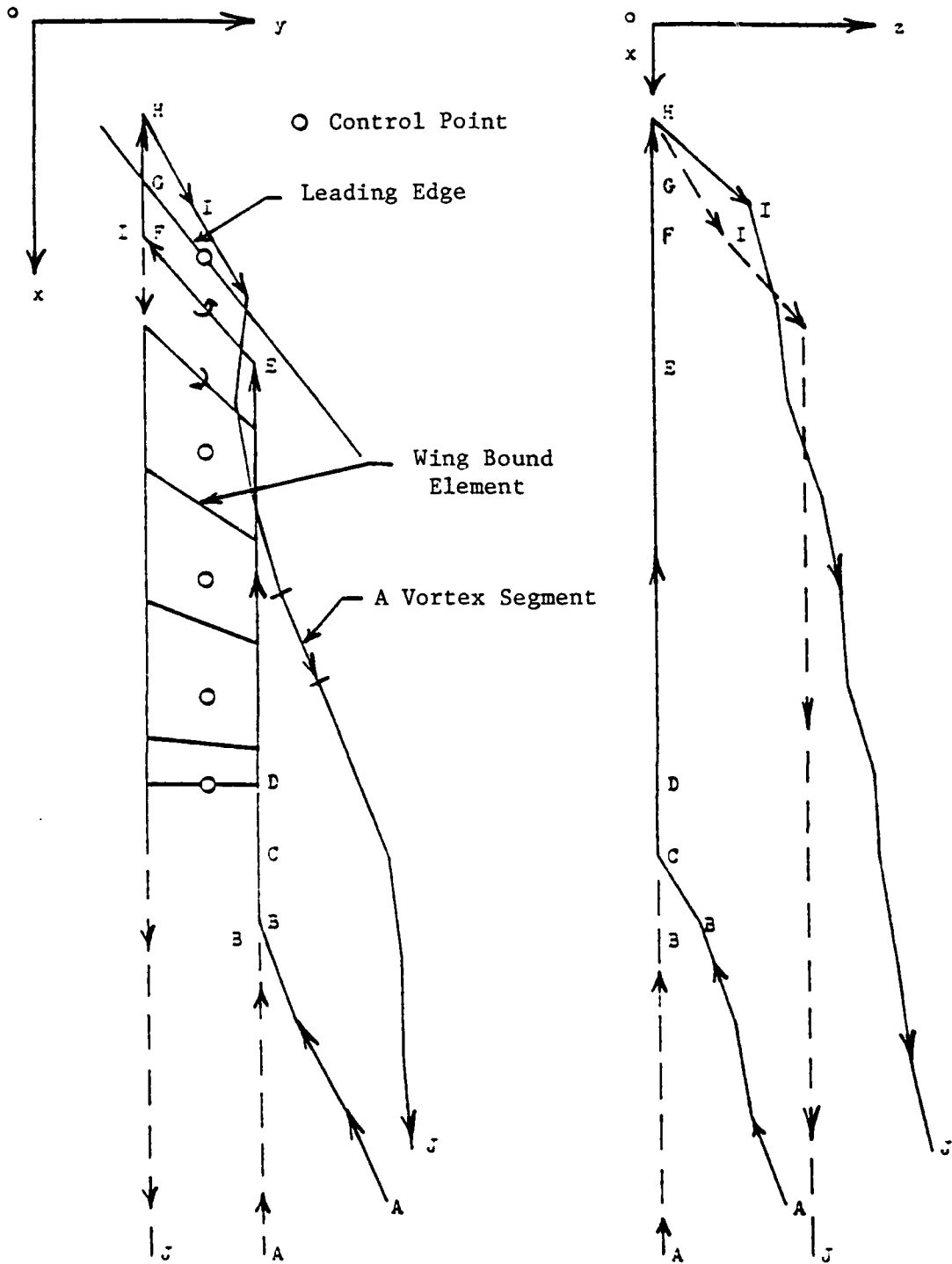


Figure 5. A Typical Vortex Element of Leading-Edge Vortex System.

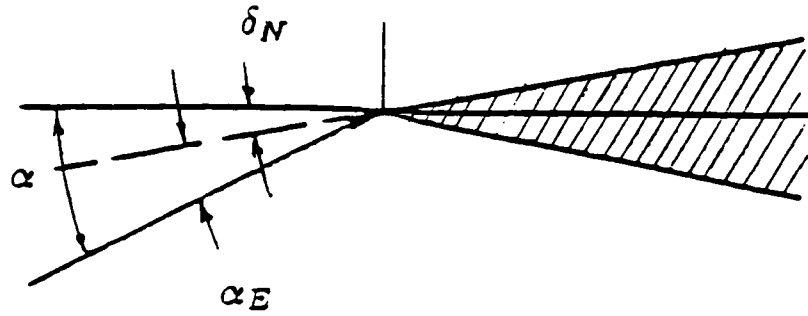
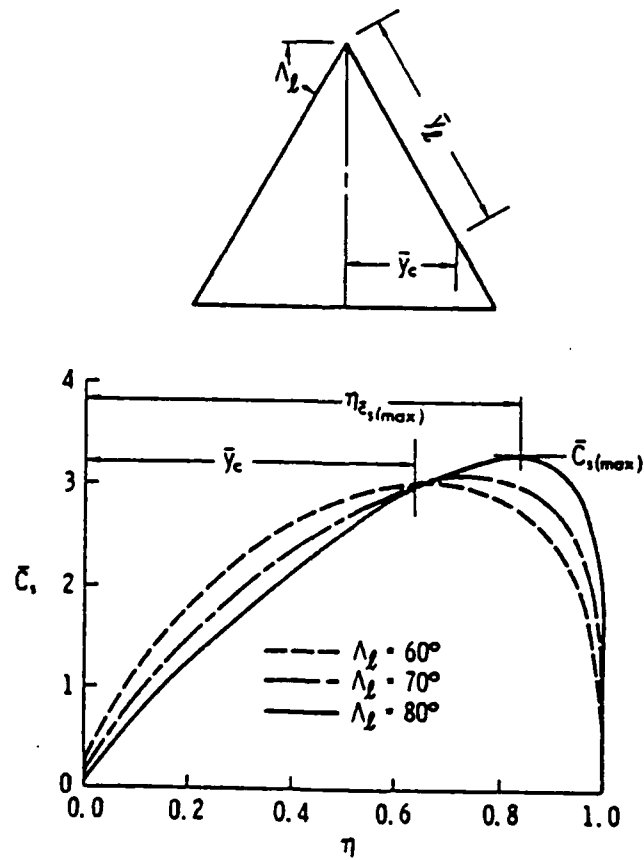
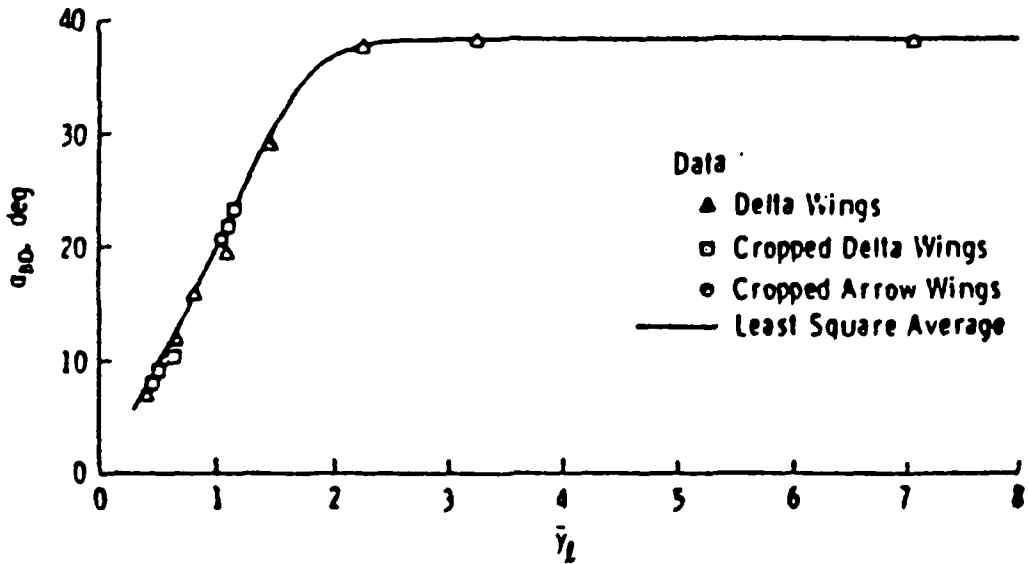


Figure 6. Effective Angle of Attack for Thick Wings

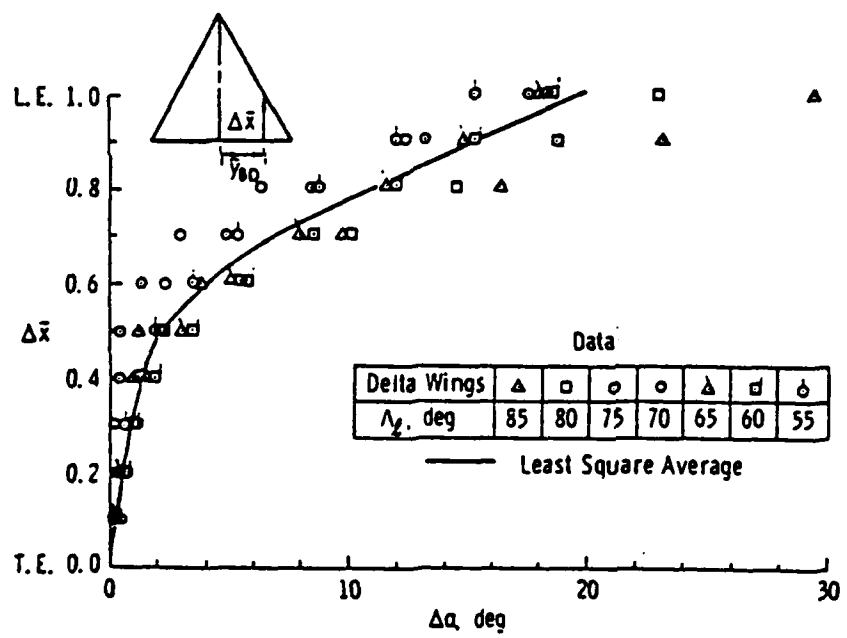


(a) Typical Leading-Edge Suction Distributions of Delta Wings with Sharp Leading Edges

Figure 7. An Empirical Model for Vortex Breakdown Effect (Ref. 25)



(b) Correlation for Angles of Attack with Vortex Breakdown at the Trailing Edge



(c) Progression of Vortex-Breakdown Points for Delta Wings in Air

Figure 7. Concluded.

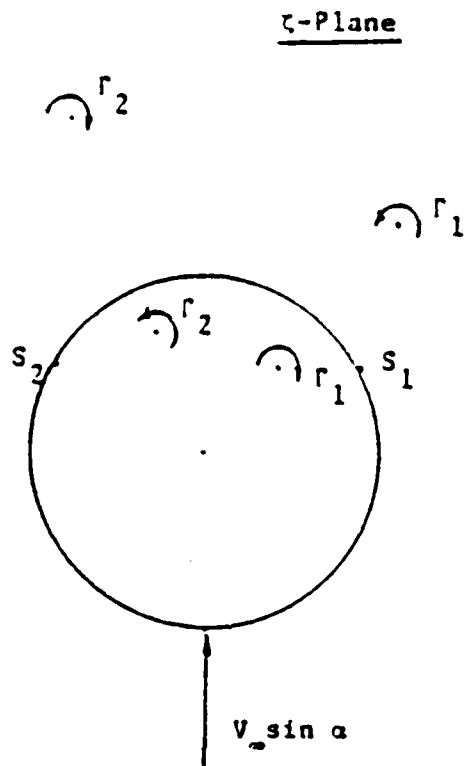


Figure 8. Vortex Separation on a Circular Cross Section

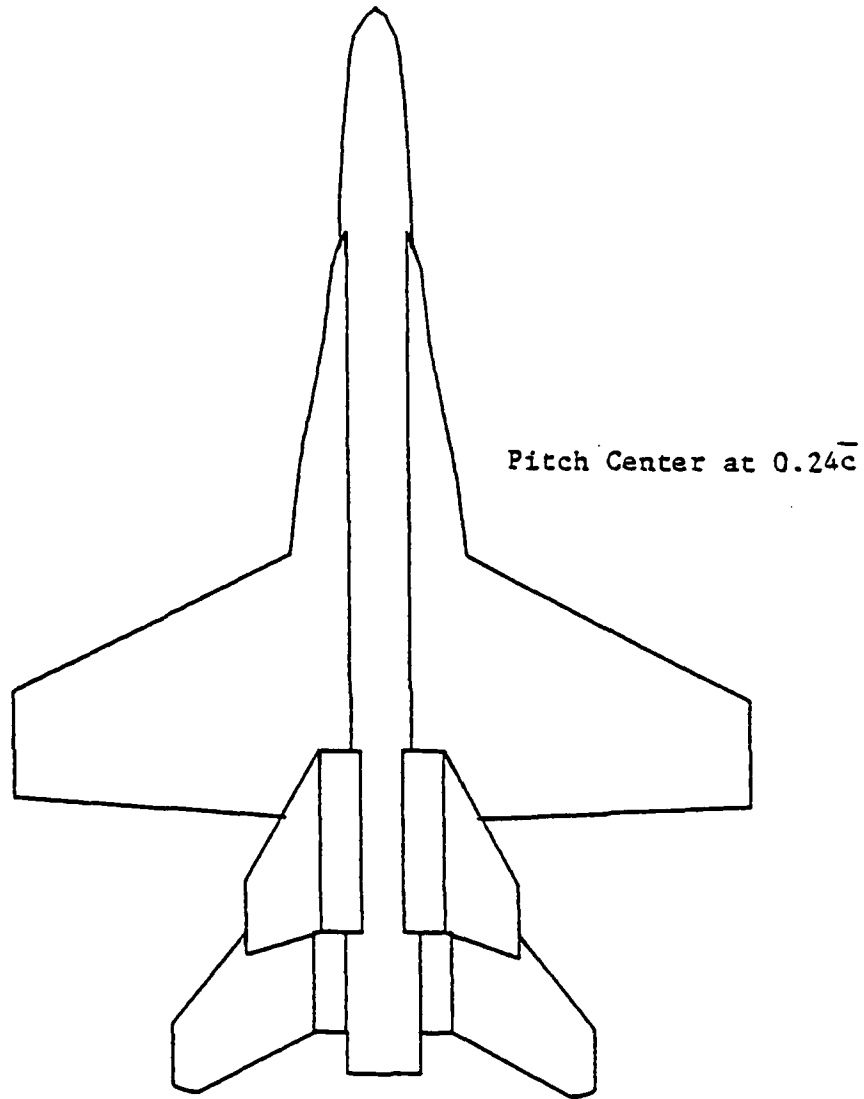


Figure 9. A Geometric Model for an F/A-18 Configuration

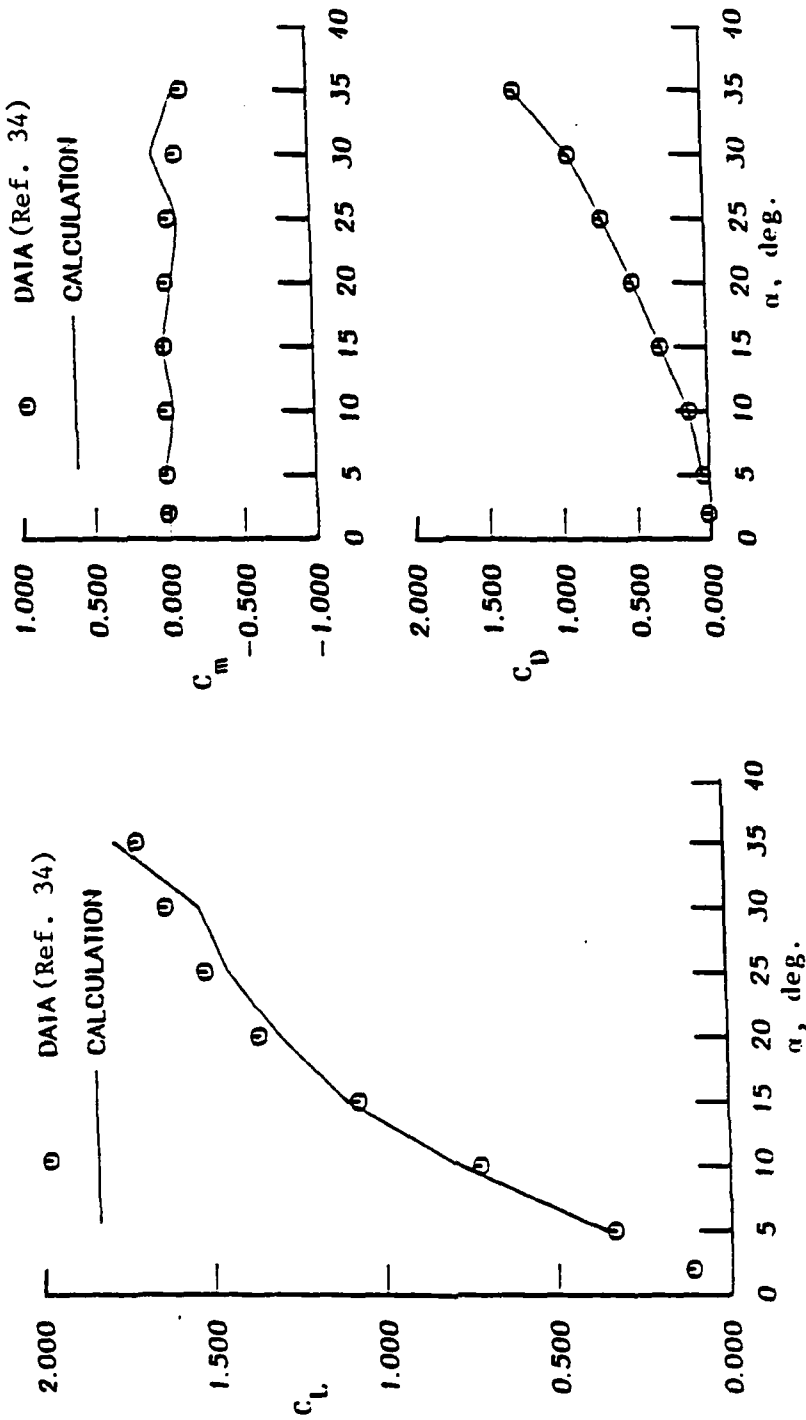


Figure 10. Longitudinal Characteristics of an F/A-18 Configuration.
 $M = 0.2, R_N = 0.6 \times 10^6$

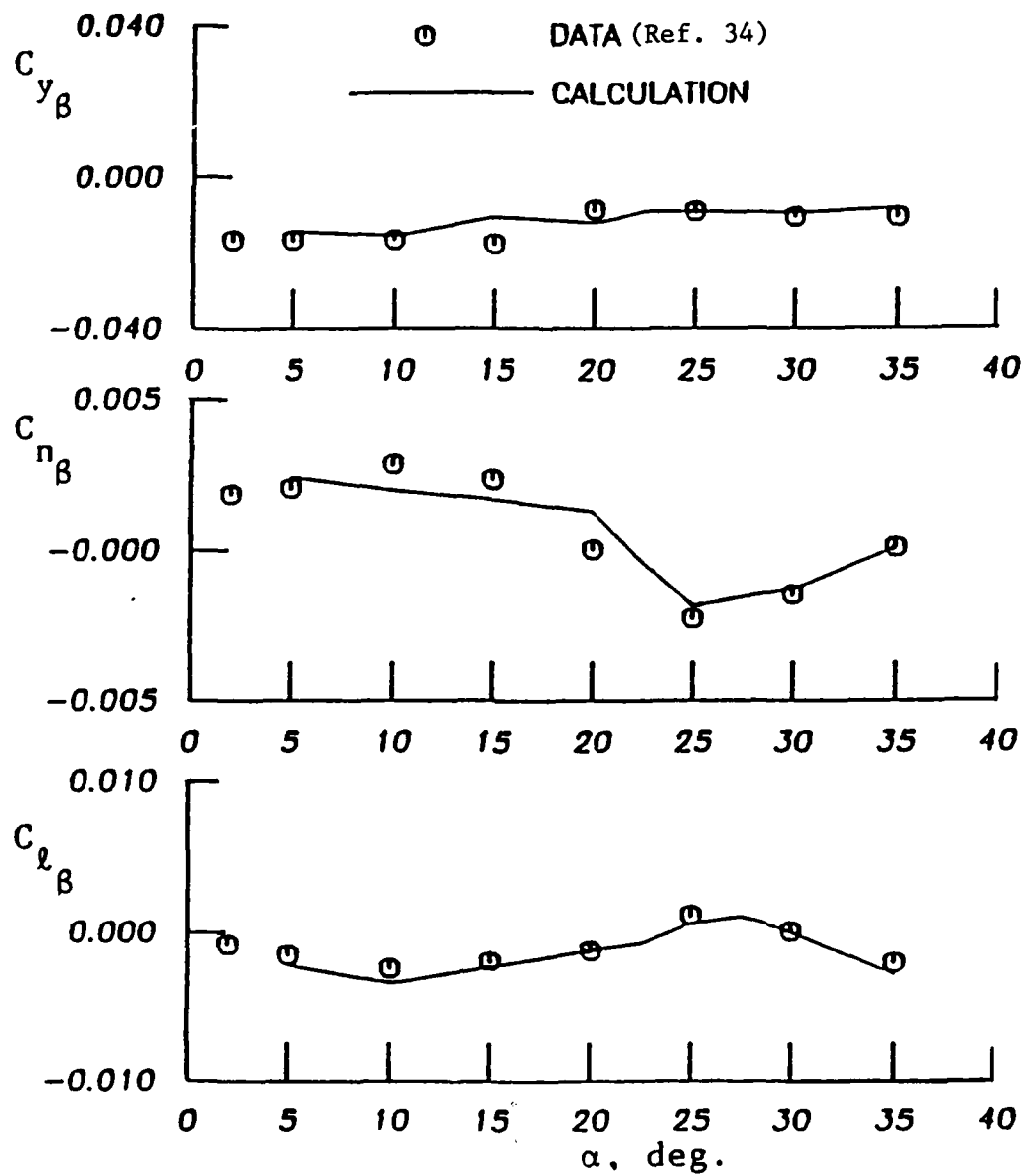


Figure 11. Sideslip Derivatives for an F/A-18 Configuration. $M = 0.2$, $R_N = 0.6 \times 10^6$
Based on Body Axes.

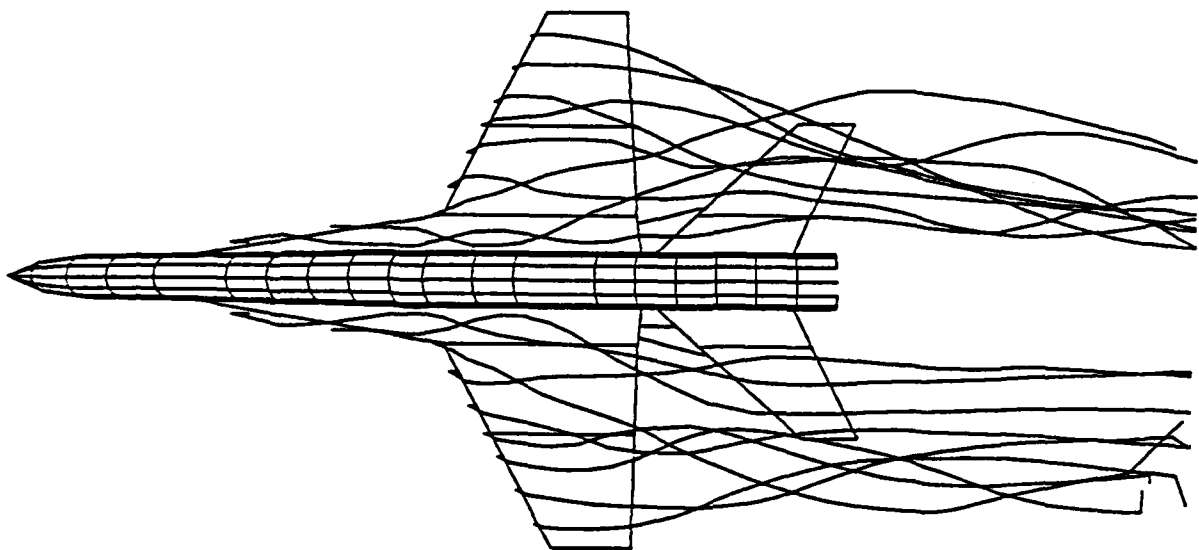
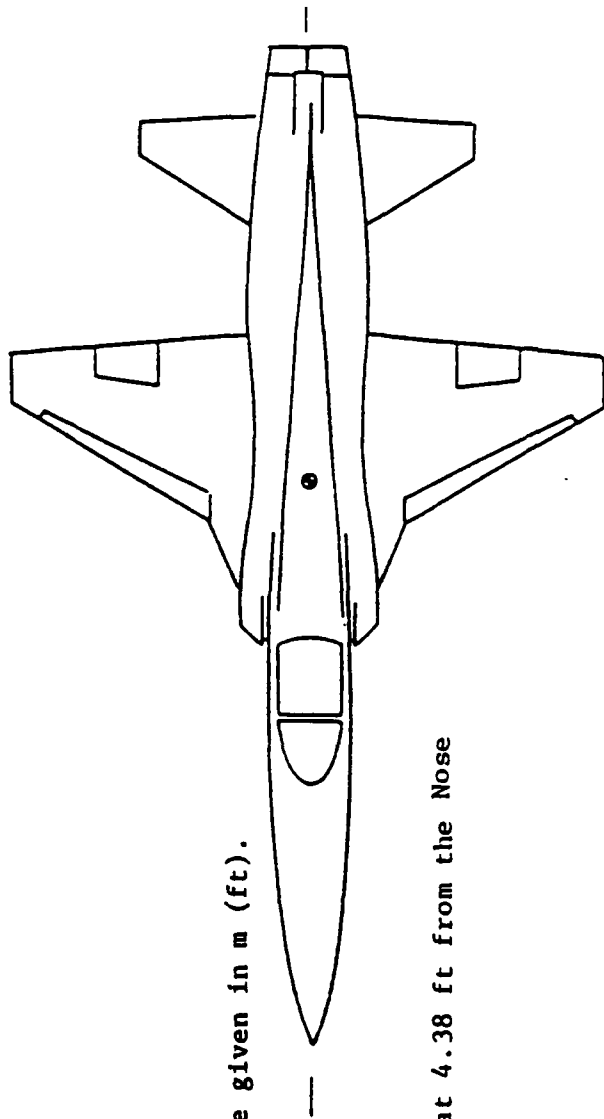


Figure 12. Vortex System for an F/A-18 Configuration at
an Angle of Attack of 25 deg. and $M = 0.2$.



Dimensions are given in m (ft).

Moment Center at 4.38 ft from the Nose

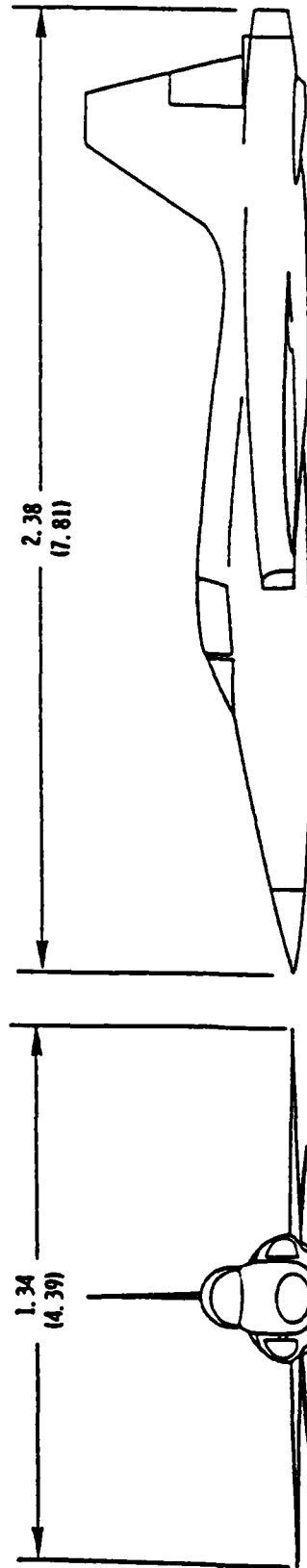


Figure 13. Three-View Sketch of an F-5 Configuration (Ref. 37)

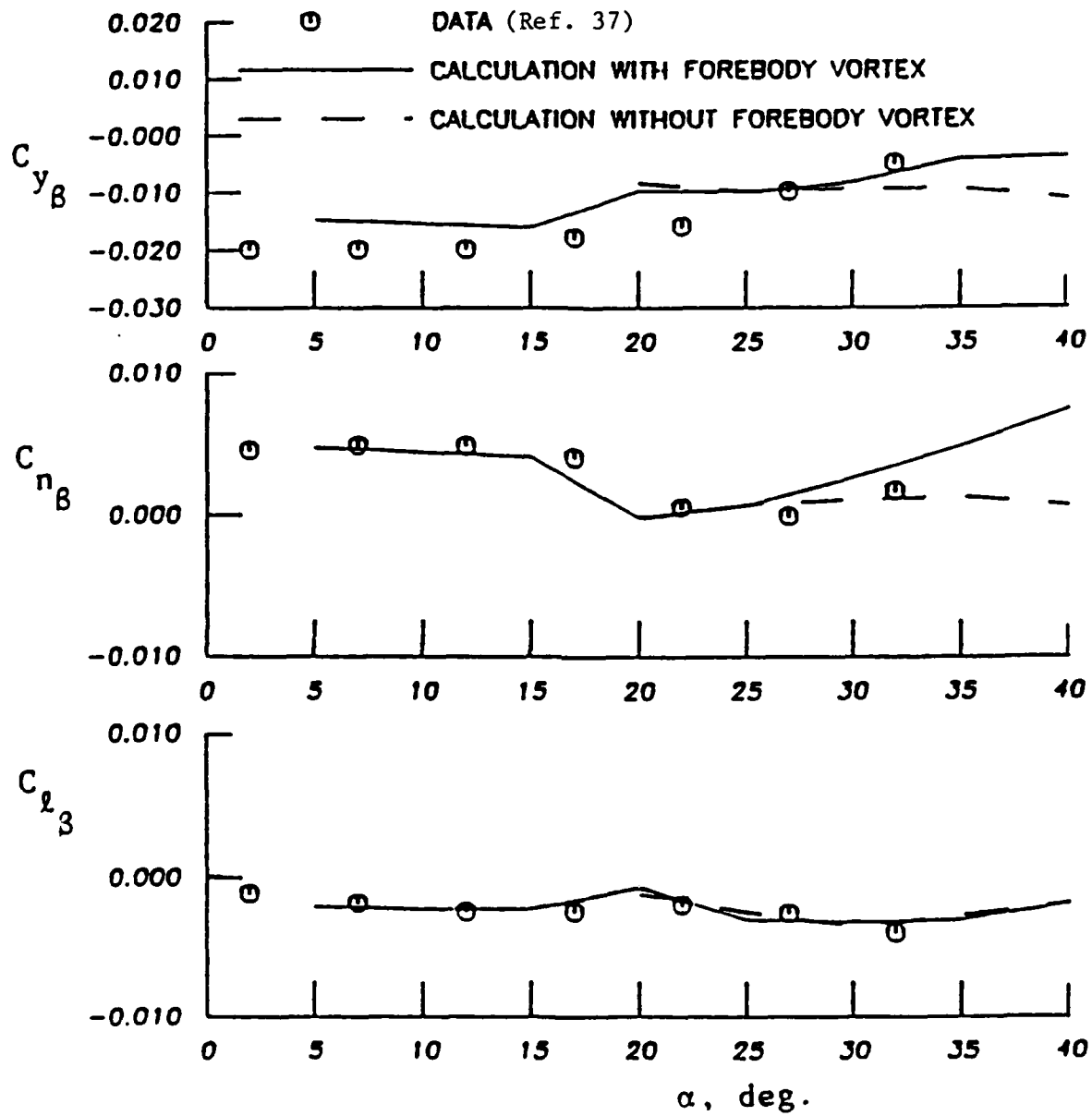


Figure 14. Sideslip Derivatives of an F-5 Configuration at $M = 0.1$ and $R_N = 0.56 \times 10^6$ Based on Body Axes.

Dimensions are given in feet.

Moment Center at $0.45\bar{c}$

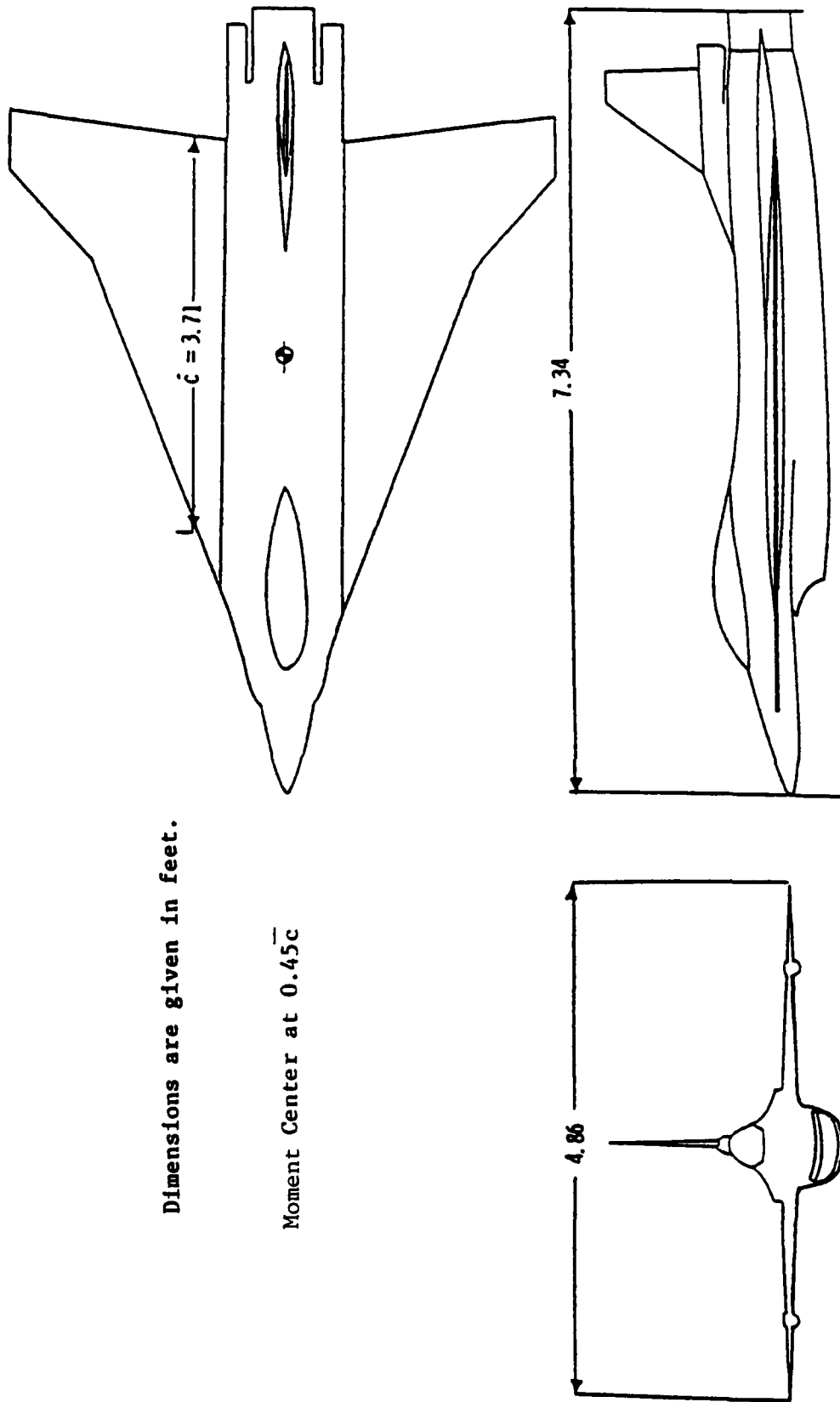


Figure 15. Three-View Sketch of an F-16XL Model (Ref. 39)

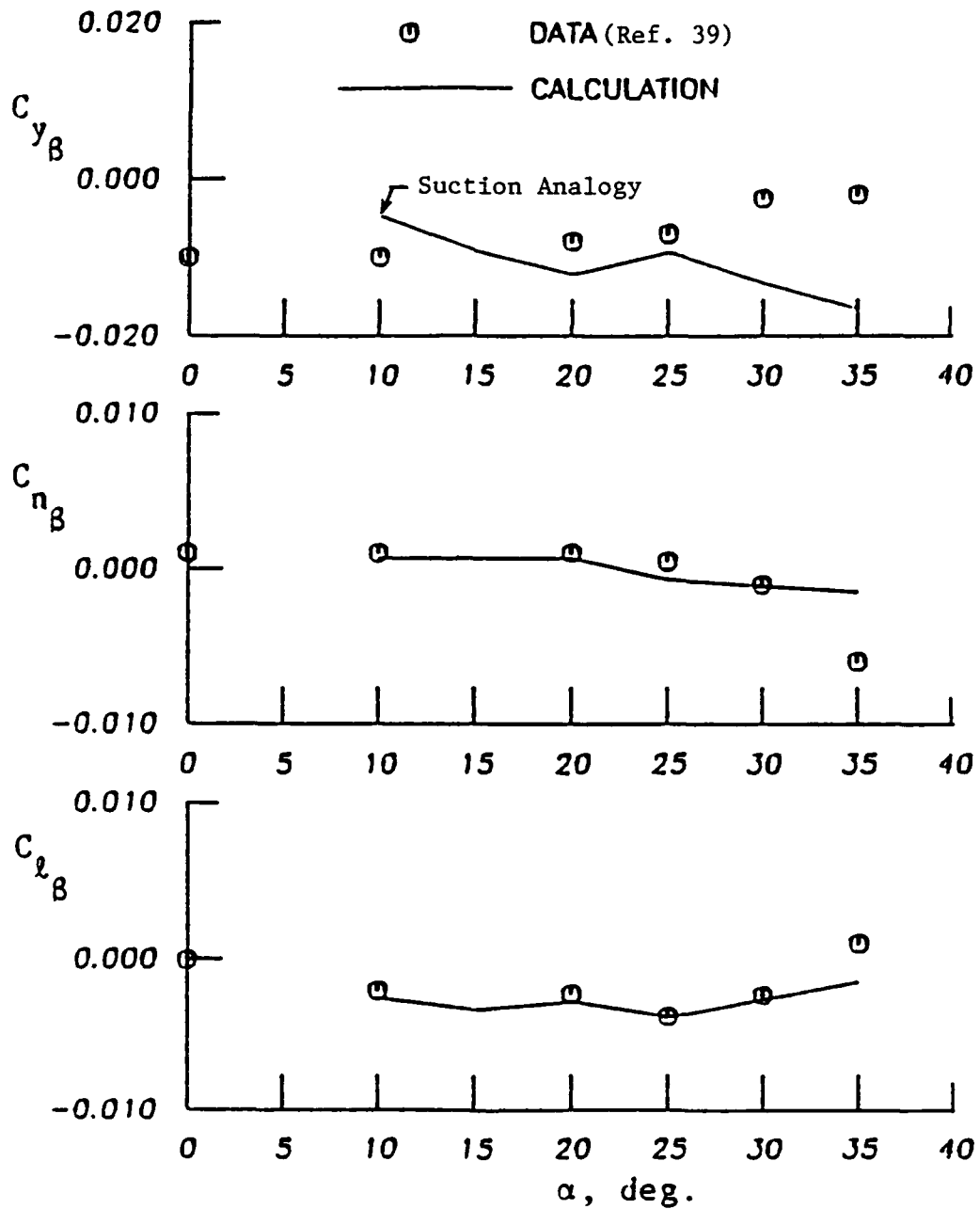


Figure 16. Sideslip Derivatives of an F-16XL Configuration at $M = 0.1$ and $R_N = 2.15 \times 10^6$ Based on Body Axes.

Wing area, 15.70 ft²

Span, 5.72 ft

$\bar{c} = 3.56$ ft

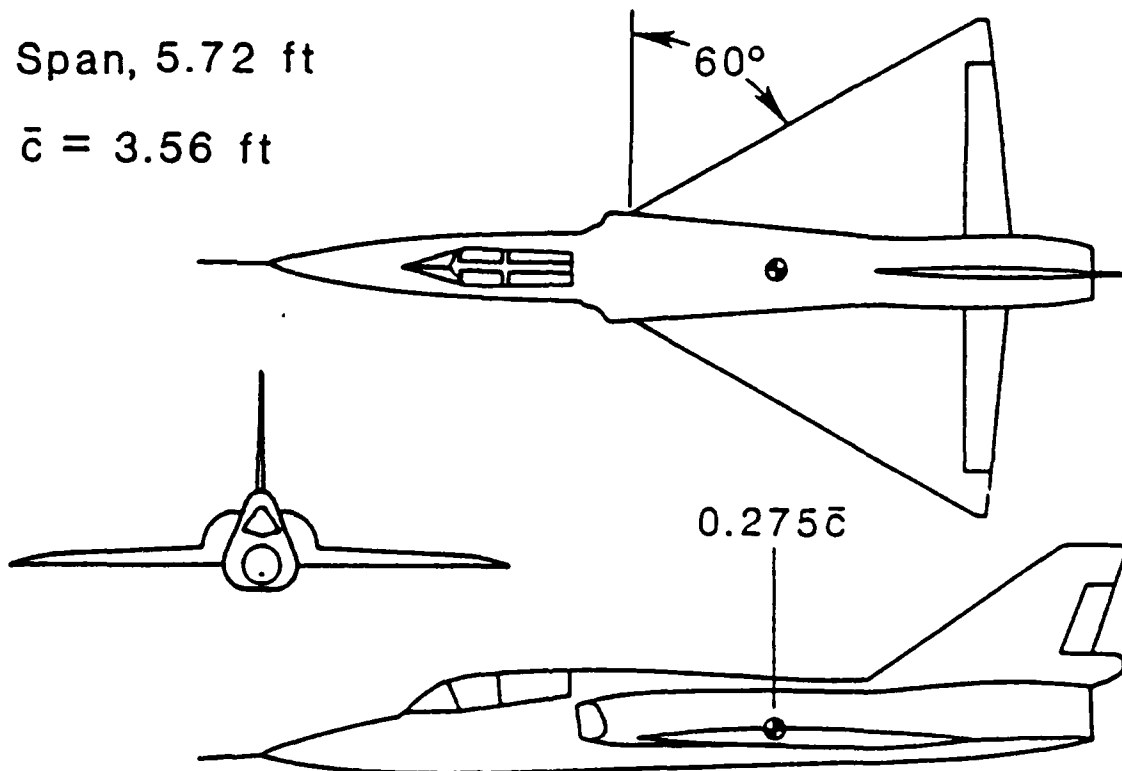


Figure 17. Three-View Sketch of an F-106B Model (Ref. 40)

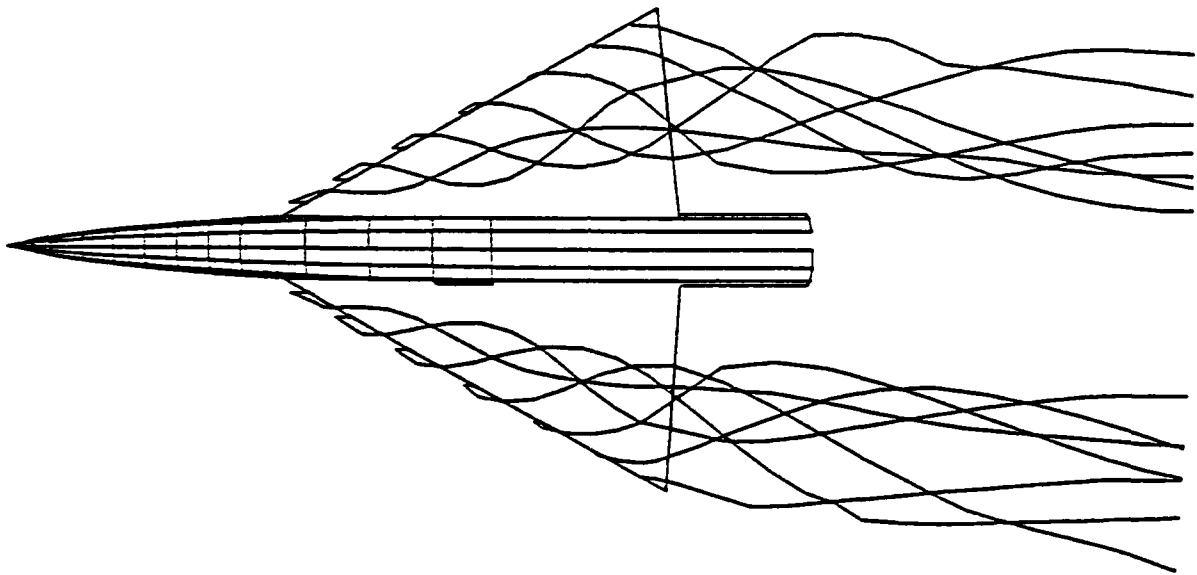


Figure 18. Vortex System for an F-106B Configuration at an Angle of Attack of 25 deg. and $M = 0.1$.

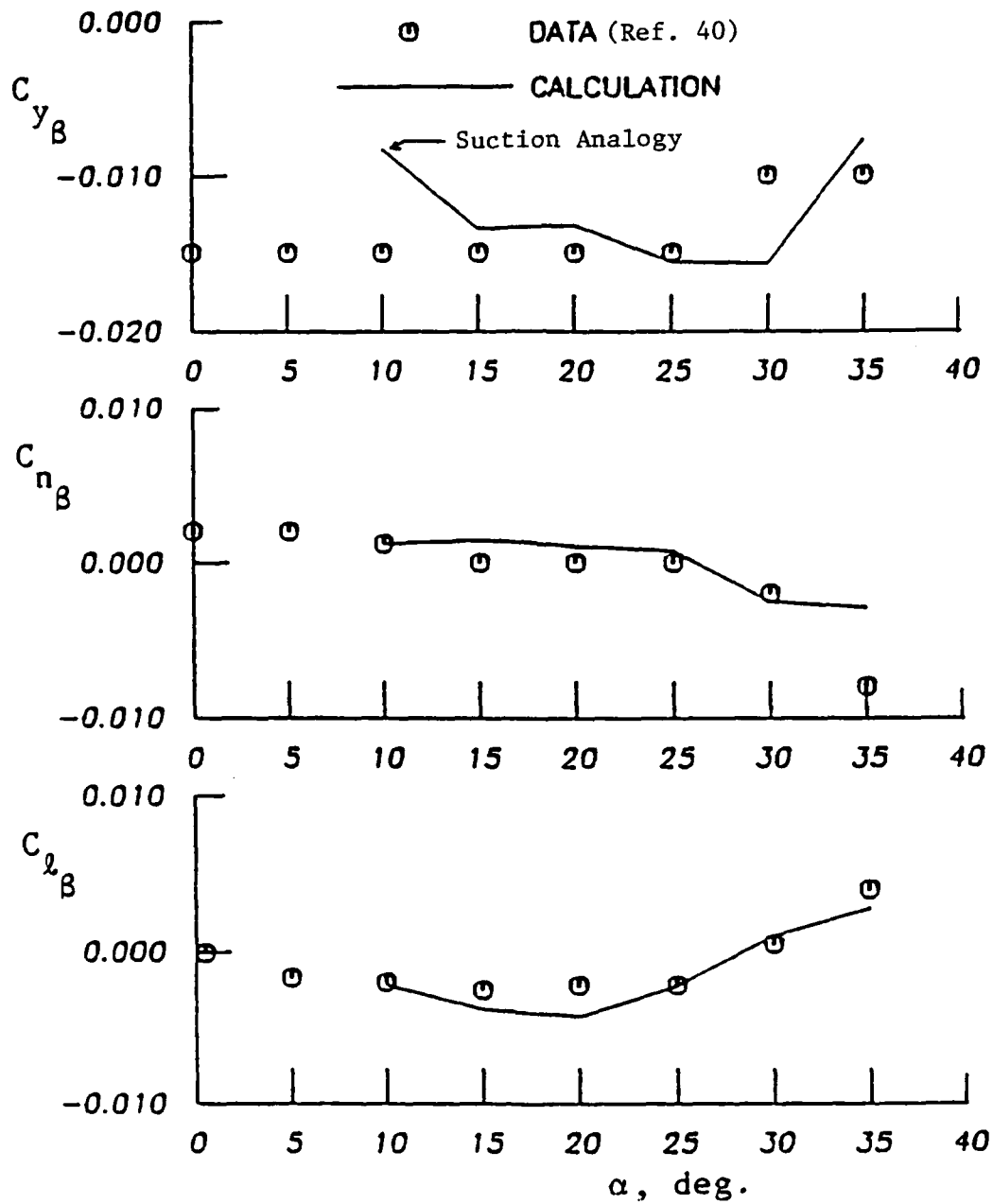


Figure 19. Sideslip Derivatives for an F-106B Configuration at $M = 0.1$ and $R_N = 10^6$ Based on Body Axes.

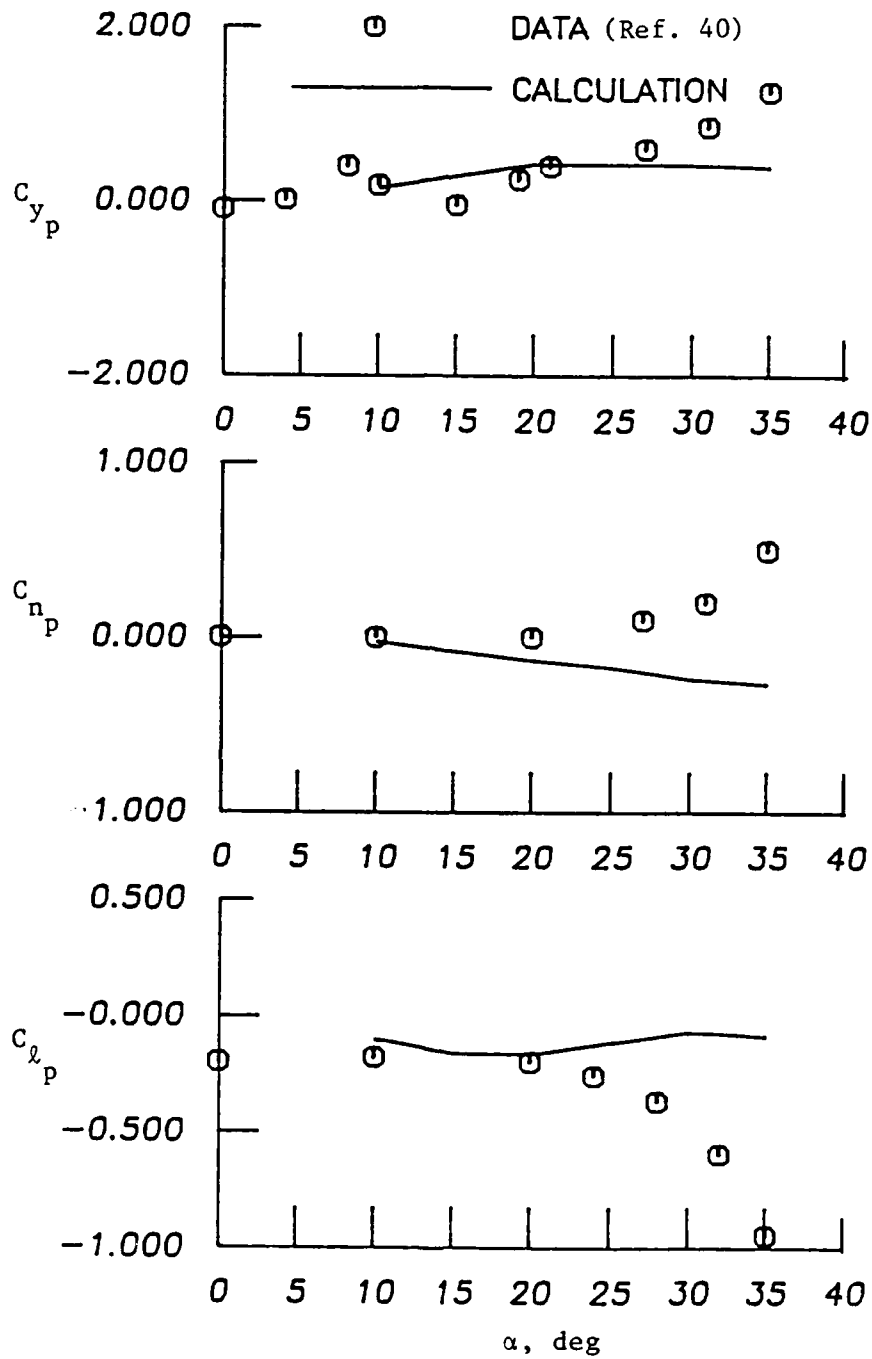


Figure 20. Lateral-Directional Derivatives for an F-106B Configuration at $M = 0.1$ and $R_N = 10^6$ Based on Stability Axes.

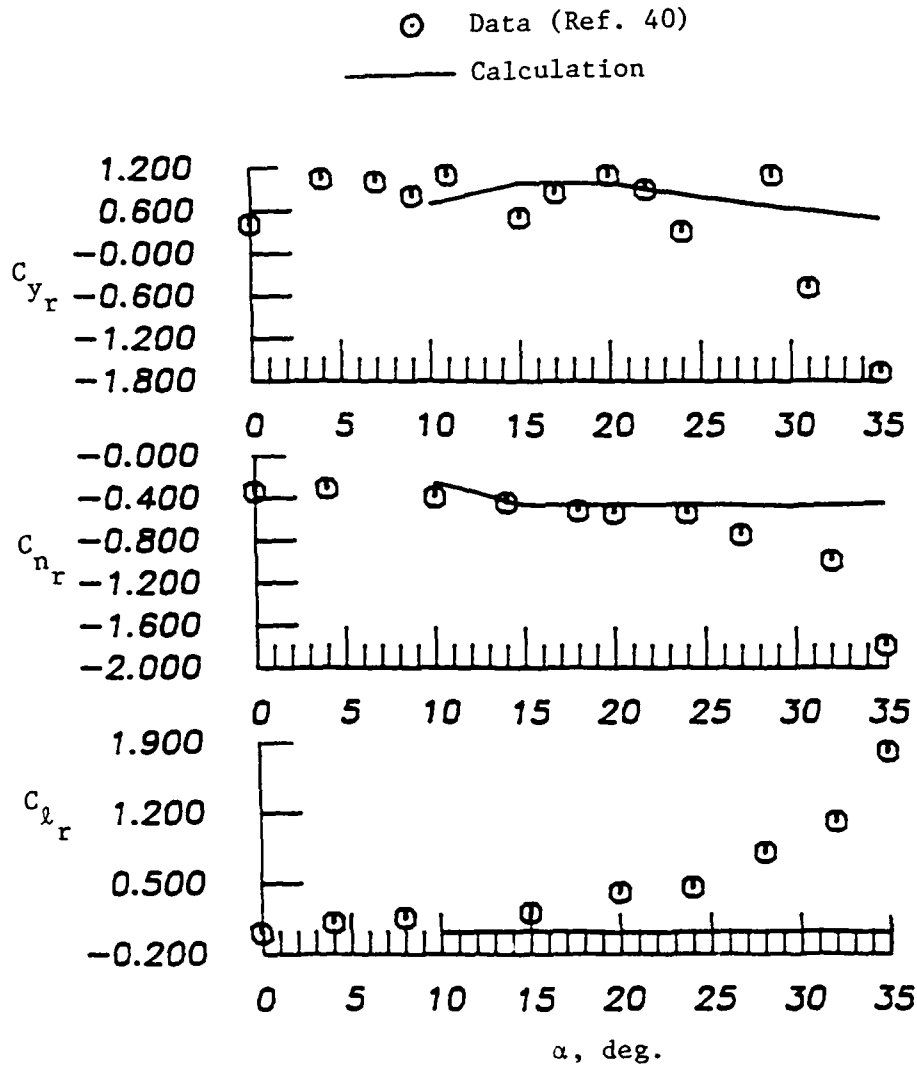


Figure 21. Lateral-Directional Derivatives for an F-106B Configuration at $M = 0.1$ and $R_N = 10^6$ Based on Stability Axes.